Nano Convergence

FULL PAPER Open Access

An interstitial fluid-like NICHE-chip for neural stem cell niche modeling and nanoscale neurotrophic delivery

Surim Shim[1†], Yejin Lee[1†], Hyun Lee[2†], Nayoung Lee[3], Da Eun Kim[4], Jongsoo Han[1], Kang Moo Huh[4,5*], Hyun-Do Jung[3*] and Kisuk Yang[1,6,7*]

Abstract

Neural stem cells (NSCs) reside in anatomically confined niches, where three-dimensional (3D) geometry and interstitial fluid (ISF) flow collectively regulate NSC behavior. However, in vitro platforms that simultaneously recapitulate size-controlled 3D architecture, ISF-like dynamics, and nanoscale therapeutic delivery remain limited. Here, we present a 3D printing-based platform with multi-sized microwells, termed the Neural-Inspired Culture for a Hydrodynamic Environment (NICHE)-chip, which incorporates an osmosis-driven flow system to generate ISF-like flow. The NICHE-chip enabled stable formation of uniform human neural stem cell (hNSC) neurospheres across defined microwell sizes. Under ISF-like flow, hNSC neurospheres showed enhanced viability, reduced apoptosis, and increased self-renewal and differentiation marker expression, particularly in 100 μm microwells. ISF-like flow also promoted laminin-rich extracellular matrix (ECM) deposition and cell–cell interactions, suggesting niche-like remodeling of the 3D microenvironment. In the ISF-integrated 100 μm neurosphere model, amyloid-β (Aβ) was introduced to establish an Alzheimer's disease (AD)-like neurotoxicity model, which was then used to evaluate nanoparticle-mediated neurotrophic factor delivery using brain-derived neurotrophic factor (BDNF)-loaded poly(lactic-co-glycolic acid) (PLGA) nanoparticles. BDNF-loaded PLGA nanoparticles (BDNF-NPs) enabled sustained BDNF delivery, attenuated Aβ-induced neuronal marker loss, and counter-regulated a subset of Aβ-induced transcriptional alterations associated with neuroprotection. Overall, the NICHE-chip provides an ISF-integrated 3D neurosphere culture platform for NSC niche modeling, AD-like neurotoxicity assessment, and nanoscale neurotrophic factor delivery.

Keywords Microfluidic platform, Osmotic pump-driven flow, Neural stem cells, Neurodegenerative disease modeling, 3D printing, Nanoparticle-mediated delivery

†Surim Shim, Yejin Lee and Hyun Lee contributed equally to this work.

*Correspondence:
Kang Moo Huh
khuh@cnu.ac.kr
Hyun-Do Jung
hdjung@hanyang.ac.kr
Kisuk Yang
kisuky@inu.ac.kr

Full list of author information is available at the end of the article

© The Author(s) 2026. **Open Access** This article is licensed under a Creative Commons Attribution-NonCommercial-NoDerivatives 4.0 International License, which permits any non-commercial use, sharing, distribution and reproduction in any medium or format, as long as you give appropriate credit to the original author(s) and the source, provide a link to the Creative Commons licence, and indicate if you modified the licensed material. You do not have permission under this licence to share adapted material derived from this article or parts of it. The images or other third party material in this article are included in the article's Creative Commons licence, unless indicated otherwise in a credit line to the material. If material is not included in the article's Creative Commons licence and your intended use is not permitted by statutory regulation or exceeds the permitted use, you will need to obtain permission directly from the copyright holder. To view a copy of this licence, visit http://creativecommons.org/licenses/by-nc-nd/4.0/.

Graphical abstract

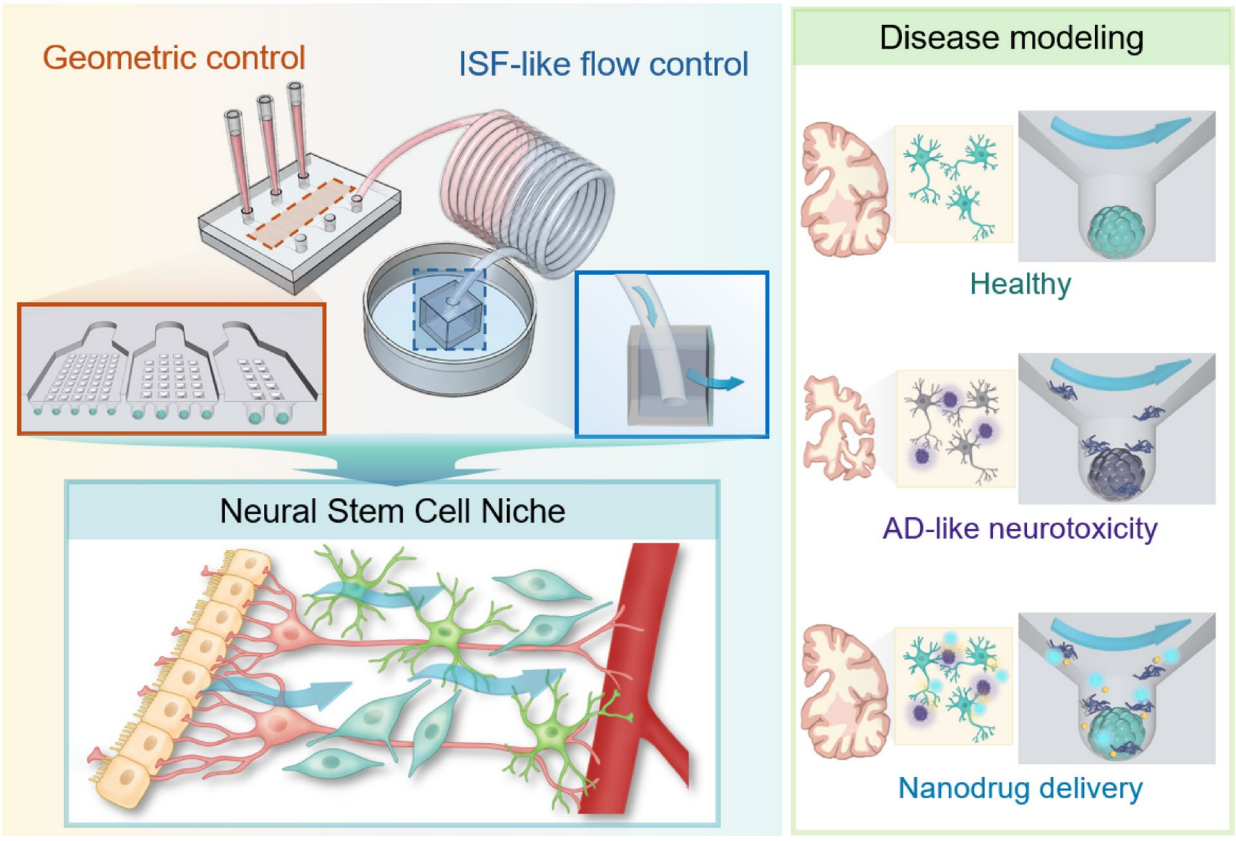

1 Introduction

Neural stem cells (NSCs) reside within highly specialized anatomical niches in the brain that are essential for maintaining their unique functional properties [1, 2]. In particular, the subventricular zone (SVZ) is recognized as a major neurogenic region. Anatomically, ventricular zone–associated neurogenic regions, including the SVZ, exhibit a multilayered organization, in which neurogenic layers spanning approximately 100–300 μm in thickness harbor neural stem and progenitor cells, serving as key regions responsible for sustained neurogenesis [3, 4]. Within this region, interstitial fluid (ISF) flows through the extracellular matrix (ECM) at extremely low velocities [5]. In the brain, ISF dynamics are driven in part by hydrostatic and osmotic pressure gradients across the cerebrovascular endothelium, producing sustained low-velocity convective flow within neural tissue [6, 7]. This low-velocity convective transport supports nutrient and waste exchange throughout the NSC niche and also contributes to the regulation of self-renewal and differentiation [8, 9]. In particular, ISF helps maintain self-renewal by enhancing the delivery of mitogens, such as basic fibroblast growth factor (bFGF) and epidermal growth factor (EGF), which are essential for sustaining proliferative capacity [7, 10–15]. Given its physiological significance, precise recapitulation of both the anatomical architecture and ISF dynamics of the NSC niche is a key requirement for advanced in vitro neural models, necessitating platforms that enable precise control over geometric and hydrodynamic conditions.

Alzheimer's disease (AD), a representative neurodegenerative dementia, is characterized by progressive and irreversible neuronal loss accompanied by cognitive decline [16, 17]. Despite its increasing prevalence, disease-modifying therapies (DMTs) remain limited, highlighting the need for advanced disease models that more accurately recapitulate pathological microenvironments. In this context, accumulating evidence suggests that SVZ-resident NSCs and their niche are functionally compromised in AD, implicating impaired adult neurogenesis in disease progression [18, 19]. However, AD research still relies heavily on preclinical animal models, which exhibit limited clinical translatability due to interspecies differences [20, 21]. In vitro models offer complementary advantages by enabling cross-validation with preclinical studies and facilitating high-throughput drug screening [22–24]. Nevertheless, most existing in vitro AD models have not fully recapitulated disease-relevant

NSC responses. Previous studies have generally been conducted using single-sized spheroids or non-optimized three-dimensional (3D) structures [25] and therefore have not adequately evaluated the effects of geometric confinement within the NSC niche. In particular, the lack of integrated control over ISF-like flow and defined neurosphere geometry has limited the ability of these systems to precisely reproduce the cellular behavior and toxic responses observed in the native niche. In addition, in static culture-based models, the local distribution and exposure of amyloid-β (Aβ) oligomers may become heterogeneous [26], which can lead to underestimation or overestimation of neurotoxicity.

Precise in vitro modeling, as a primary requirement, relies on 3D culture platforms that recapitulate key structural features of the niche [27]. Stem cell spheroids are widely used to model tissue-like 3D structures in vitro, as their size and shape influence cellular behavior, including self-renewal and differentiation [28–33]. In the case of NSCs, these cell aggregates are specifically referred to as neurospheres, which serve as essential in vitro models for studying neural development, differentiation, and disease pathology [29, 30]. Like other spheroids, neurosphere size can influence cellular fate by affecting cell–cell interactions, mass transport, self-renewal, and differentiation [31, 32, 34]. Therefore, a platform capable of systematically modulating spheroid size within a single batch is crucial for generating physiologically relevant neurospheres and advancing studies on NSC behavior. Traditionally, the hanging-drop method has been used to generate spheroids by suspending uniform droplets through surface tension. However, the process is labor-intensive and offers limited scalability for high-throughput screening [33, 35–37]. As an alternative approach, multi-well systems have been developed, allowing for better control over spheroid diameter [31, 38, 39]. However, these systems do not enable simultaneous modulation of well depth within a single batch, thereby limiting the formation of geometrically consistent neurospheres of varying sizes. Because spheroid shape can influence diffusion distances and the distribution of oxygen, nutrients, and soluble factors, variations in sphericity may confound the interpretation of geometry-dependent cellular responses [40, 41]. Thus, simultaneous control of neurosphere diameter and height is required to generate geometrically consistent spheroids and to enable systematic comparison of their effects on cellular behavior.

Although 3D culture systems can recapitulate native tissue architecture, conventional static cultures remain limited by diffusion-dependent mass transport. Thus, dynamic culture or perfusion systems are required to more closely reproduce physiologically relevant in vivo-like microenvironments [42, 43]. In the field of microfluidics, simple rocker-based strategies have been used to provide flow within the cellular microenvironment. However, these systems are limited by the fact that they generate bidirectional flow [44]. Syringe pumps have also been widely used because they can provide uniform unidirectional flow. However, their reliance on external equipment and tubing increases system complexity and may limit scalability for long-term, high-throughput applications.

To address these limitations, we developed a culture platform, termed the Neural-Inspired Culture for a Hydrodynamic Environment (NICHE)-chip. Our NICHE-chip features multi-well structures with size-specific widths and depths, fabricated through a one-step digital light processing (DLP) printing-based mold fabrication process. Unlike conventional multi-well systems, this design enables the simultaneous formation of spherical neurospheres of different sizes within a single batch, facilitating efficient comparison and monitoring of size-dependent cellular behavior. Furthermore, inspired by the fact that the slow movement of ISF is regulated by combined hydrostatic and osmotic gradients [6, 7], an osmosis-driven flow system was integrated into the NICHE-chip. This osmosis-driven system exploits osmotic pressure generated by fluid movement across a semipermeable membrane in the presence of polymeric solutes, thereby providing continuous low flow rates on the order of tens of μL/h without external power [39, 40].

Using this platform, we examined how ISF-like flow and well size regulate human neural stem cell (hNSC) self-renewal, differentiation, extracellular matrix production, and cell–cell interactions. Using the 100 μm neurosphere condition under NICHE-ISF, we further established an Aβ-induced AD-like neurotoxicity model and evaluated the efficacy of a therapeutic intervention, thereby validating the platform for drug screening and therapeutic assessment. Brain-derived neurotrophic factor (BDNF) was selected as a test molecule based on its well-established neuroprotective effects against Aβ-induced neurotoxicity [45–47]. However, direct administration of soluble BDNF is limited by its short biological stability and rapid degradation or clearance in dynamic microenvironments, which may restrict sustained therapeutic efficacy [48–50]. Thus, BDNF was loaded into biodegradable poly(lactic-co-glycolic acid) (PLGA) nanoparticles to enable sustained delivery, and the neuroprotective effects of BDNF-loaded PLGA nanoparticles (BDNF-NPs) were evaluated within the NICHE-chip. Transcriptomic analysis provided molecular insights into the underlying neurotoxic and neuroprotective responses.

These findings suggest that the NICHE-chip can recapitulate key features of the NSC niche and has potential as a platform for evaluating drug-delivery strategies, including sustained nanoparticle-based neurotrophic factor delivery. Although the current system is designed

primarily for detailed condition-specific analyses, it could be further adapted for high-throughput applications, enabling large-scale investigations of stem cell behavior under precisely controlled culture conditions.

2 Materials and methods

2.1 Fabrication of a 3D-printed multi-well device

The multi-well device was designed using computer-aided design (CAD) software and a DLP 3D printer (Asiga PICO2 HD, Asiga, AUS). A photocurable solution consisting of tert-butyl acrylate (tBA, Merck, USA) and 1,6-hexanediol diacrylate (HDDA, Merck, USA) was utilized [51]. The 3D-printed structure was subsequently used as a mold for polydimethylsiloxane (PDMS; Dow Corning, MI, USA) casting to fabricate the bottom layer for the multi-well chamber. Then, the chamber was finally bonded to the top layer containing the inlet and outlet using oxygen plasma treatment (1 min, 100 W) with a Plasma System (Femto Science Inc., HwaSeong, Republic of Korea) to establish a 100 μm-high 3D microenvironment.

2.2 Osmotic system setup for modeling ISF-like flow

The design of the osmotic system was adapted from a previously established protocol [52]. Briefly, the osmotic system was constructed by attaching a semipermeable cellulose membrane to a resin cube reservoir filled with distilled water, with an osmotic pressure gradient generated by polyethylene glycol (PEG) outside the membrane. The reservoir was designed by cutting acrylic using a laser cutter (ML-6040X, Machine Shop, Paju, South Korea), molding with PDMS, and curing resin in the mold. PEG 1000 (Thermo Fisher Scientific, MA, USA) was melted in a 50 °C water bath until fully liquefied, and then preheated deionized (DI) water was gradually added with gentle stirring to prepare a final concentration of 0.5 M. Subsequently, the reservoir was immersed in a dish containing the prepared 0.5 M PEG solution to generate an osmotic pressure gradient. The tubing (AAD04119; Tygon, Courbevoie, France) connected to the reservoir was linked to the outlet of the device, while a pipette tip containing culture medium was inserted into the inlet, allowing continuous medium flow through the device. To quantify the resulting flow rate, changes in the internal weight of the cube reservoir were monitored over time. The cube was weighed at defined intervals during osmotic operation under a 0.5 M PEG condition. The measured weight change was converted to volumetric flow assuming a water density of 1 g/mL, allowing estimation of the average flow rate generated by the system. For static culture conditions, the device was operated without connecting tubing to the outlet and a pipette tip to the inlet.

2.3 Cell culture

hNSCs (ReNCell VM) were purchased from Sigma-Aldrich (MA, USA). Cells were cultured according to the manufacturer's protocol. Before seeding, a T-75 flask was coated with 5 mL laminin protein solution (10 μg/mL; Corning, NY, USA) and incubated for at least 2 h at 37 °C with 5% CO_2 in a humidified incubator. The hNSCs were maintained in Dulbecco's Modified Eagle's Medium/Nutrient Mixture F-12 (DMEM/F-12; Gibco, Waltham, USA), containing 1% N-2 supplement (100X; Thermo Fisher Scientific), 2% B-27 supplement (50X; Thermo Fisher Scientific) and 2% Penicillin-Streptomycin (P/S, Gibco). For proliferation conditions, recombinant human bFGF and EGF (R&D Systems, MN, USA) were added to the media at a final concentration of 20 ng/mL each. The culture medium was changed every 2 days, and all cells were maintained at 37 °C with 5% CO_2 in a humidified incubator. For spontaneous differentiation conditions, mitogens were removed from the medium.

2.4 hNSCs seeding in the device

Before seeding hNSCs into the device, the wells were coated with 0.1 wt% hexanoyl glycol chitosan (HGC) solution. HGC with a degree of hexanoyl substitution of 36% was selected based on previous reports demonstrating its enhanced coating stability [53]. After filling the microwells with the HGC solution, air bubbles were removed to ensure complete contact between the microwell surfaces and the HGC solution and the device was incubated at room temperature for 30 min. The solution was then removed by aspiration, and the device was placed in an oven at 60 °C overnight to allow complete coating. The HGC-coated device was washed three times with Dulbecco's phosphate-buffered saline (DPBS, Welgene, Daegu, Korea). Then, hNSCs were seeded at a density of 1.5×10^7 cells/mL and incubated at 37 °C in a humidified atmosphere with 5% CO_2 for 30 min. To maintain a uniform hNSC seeding density across different well depths, the number of wells per condition was adjusted to ensure consistent total cell loading. After 30 min, unsettled cells were gently washed out using DPBS. The culture medium was replaced with the aforementioned medium composition, and cells were subsequently cultured under the previously described conditions. After cell seeding, hNSCs in the devices were cultured under three experimental configurations: NICHE-macro, where the microwell chip was placed in a conventional culture dish; NICHE-static, where the assembled 3D device was maintained without flow; and NICHE-ISF, where the assembled 3D device was operated under osmosis-driven ISF-like flow. All groups were cultured under proliferation conditions for 2 days, followed by 6 days under spontaneous differentiation conditions.

2.5 Computational simulation

Computational simulations were performed using COMSOL Multiphysics v6.1 (COMSOL Inc., Burlington, MA, USA) to analyze local solute transport within the NICHE microfluidic device. A three-dimensional model was constructed based on the actual device geometry. The culture medium was approximated as water at 37 °C, and solute transport was modeled using the Transport of Diluted Species interface. Diffusion coefficients were calculated using the Stokes–Einstein equation based on hydrodynamic radii reported in previous studies, yielding 2.34×10^{-10} m^2/s for EGF [54], 1.16×10^{-10} m^2/s for bFGF [55], and 2.29×10^{-11} m^2/s for oligomeric Aβ [56]. Time-dependent transport analysis was performed to evaluate local solute transport over time. The initial solute concentration within the microfluidic chip was set to zero, and solute-containing medium was introduced through the inlet. Under NICHE-static conditions, solute transport was governed by diffusion alone, whereas under NICHE-ISF conditions, the previously determined ISF-like flow rate was applied so that both diffusion and convection were considered. In addition, solute transport within the spheroid domain was assumed to occur by diffusion only, without bulk flow.

2.6 AD modeling

Synthetic Aβ1–42 peptide (Abcam, Cambridge, UK) was prepared as a 1 mM stock solution in dimethyl sulfoxide (DMSO) according to previously described protocols [57], incubated at 4 °C for 24 h and finally diluted in the culture medium to a final concentration of 5 μM for the evaluation of neurotoxic effects [58]. Based on previous reports demonstrating the neuroprotective effects of BDNF (PeproTech, NJ, USA) against Aβ-induced neurotoxicity [46–48], BDNF-loaded PLGA nanoparticles were administered at a dose corresponding to an equivalent BDNF concentration of 20 ng/mL to assess their neuroprotective efficacy. During differentiation, cells were maintained in normal differentiation medium for 3 days and subsequently cultured for an additional 3 days in either (1) normal medium, (2) medium supplemented with 5 μM Aβ, or (3) medium supplemented with 5 μM Aβ and 20 ng/mL BDNF-NPs.

2.7 Fabrication of BDNF-NP

BDNF-NPs were prepared using the emulsion solvent evaporation method based on previously reported PLGA nanoparticle fabrication protocols [59]. The morphology and size distribution of the fabricated particles were analyzed using scanning electron microscopy (SEM) images. Representative SEM images were acquired, and the diameter of individual particles was measured using ImageJ software. The measured particles were classified into predefined size ranges, and the number of particles in each range was converted into a percentage of the total number of analyzed particles to obtain the particle size distribution. To evaluate the BDNF release profile, BDNF-NPs were dispersed in DPBS and incubated at 37 °C. At predetermined time points, the samples were centrifuged, and the supernatant was collected and replaced with an equal volume of fresh DPBS. The BDNF concentration in the collected supernatant was quantified using a BDNF enzyme-linked immunosorbent assay (ELISA) kit, and the cumulative release was expressed as a percentage of the total loaded BDNF.

2.8 Cell viability test

To evaluate hNSC viability within the microenvironment of the device, neurospheres were cultured for 2 days in the presence of mitogens and subsequently assessed for viability within the device. Cell viability was evaluated using both qualitative staining with the Live/Dead™ Viability/Cytotoxicity Kit containing calcein-AM and ethidium homodimer-1 (Thermo Fisher Scientific) and quantitative analysis with the alamarBlue™ Cell Viability Reagent (Thermo Fisher Scientific), following the manufacturer's protocols. The alamarBlue™ assay was used to quantitatively assess the effect of the flow system on cell viability. Fluorescence values from all alamarBlue™ assays were normalized to those of the control group.

2.9 Immunofluorescence staining

Immunofluorescence staining was performed according to our previously reported protocol [60]. Briefly, after 8 days of culture to assess hNSC differentiation, the medium was carefully aspirated, and cells were fixed with 4% paraformaldehyde (Tech&Innovation, Chuncheon, Korea) for 30 min at room temperature. Permeabilization was then performed using 0.1% Triton X-100 (Sigma-Aldrich) in DPBS for 1 h. To block nonspecific binding, samples were incubated with 4% bovine serum albumin (BSA; Sigma-Aldrich) for 4 h at room temperature. For immunostaining, samples were incubated overnight at 4 °C with the following primary antibodies: rabbit anti-βIII tubulin (Tuj1; 1:500; Cell Signaling Technology, MA, USA), rabbit anti-microtubule-associated protein 2 (MAP2; 1:500; Cell Signaling Technology), goat anti-glial fibrillary acidic protein (GFAP; 1:500; ABclonal, MA, USA), rat anti-laminin γ-1 (1:200; Santa Cruz Biotechnology, CA, USA). After primary antibody incubation, cells were treated with Alexa Fluor 488-conjugated donkey anti-goat IgG (H + L), Alexa Fluor 488-conjugated donkey anti-rat IgG (H + L) and Alexa Fluor 647-conjugated donkey anti-rabbit IgG (H + L) secondary antibodies (Thermo Fisher Scientific), diluted 1:250 in blocking solution, for 24 h at room temperature. Nuclei were counterstained with 4′,6-diamidino-2-phenylindole (DAPI, 1 μg/mL; Sigma-Aldrich). After each step, samples were

washed three times with DPBS. Fluorescence images were acquired using an inverted fluorescence microscope (Olympus IX73; Tokyo, Japan).

2.10 Quantitative real-time polymerase chain reaction (qRT-PCR)

qRT-PCR was performed according to previously established protocols [29]. Total RNA was extracted using the MiniBEST Universal RNA Extraction Kit (Takara Bio Inc, Shiga, Japan) [61]. RNA concentrations were detected using the NanoDrop Lite Plus Spectrophotometer (Thermo Fisher Scientific). RNA from each sample was reverse-transcribed into complementary DNA (cDNA) using the PrimeScript™ 1st strand cDNA Synthesis Kit (Takara Bio Inc.). qRT-PCR analysis was performed using the QuantStudio™ 1 Real-Time PCR System (Applied Biosystems, CA, USA) with Power SYBR™ Green PCR Master Mix (Applied Biosystems) and gene-specific primers from the QuantiTect Primer Assays (Qiagen, Venlo, Netherlands). The following genes were analyzed: B-cell lymphoma 2 (*BCL2*; QT00025011), BCL2-associated X protein (*BAX;* QT00031192), *Nestin* (QT00235781), *MAP2* (QT00057358), *GFAP* (QT00081151), tubulin beta 3 class III (*TUBB3;* QT00083713), *Laminin* (*LAMC1*, QT00072142), N-cadherin (*CDH2;* QT00063196) and the housekeeping gene glyceraldehyde-3-phosphate dehydrogenase (*GAPDH*; QT00079247). Relative gene expression levels were quantified using the comparative ΔΔCt method and normalized to endogenous *GAPDH* expression.

2.11 RNA sequencing analysis

Total RNA was isolated from the samples as described in Sect. 2.10. RNA quality was assessed using an Agilent 4200 TapeStation System (Agilent Technologies, CA, USA), and RNA concentration was quantified using a Qubit fluorometer. Library preparation was performed using the QuantSeq 3' mRNA-Seq V2 Library Prep Kit FWD (Lexogen, Vienna, Austria) according to the manufacturer's instructions. Briefly, first-strand cDNA was synthesized using an oligo-dT primer containing an Illumina-compatible sequence, followed by second-strand synthesis using a random primer containing an Illumina-compatible linker sequence. The resulting double-stranded libraries were purified using magnetic beads and amplified by PCR. The final libraries were sequenced on a NextSeq 2000 system (Illumina Inc., CA, USA) using single-end 100-bp reads. Raw reads were trimmed using fastp v0.23.1 [62] and aligned to the GRCh38 reference genome using STAR v2.7.10b [63]. Gene-level read counts were quantified using featureCounts v2.0.6 [64] with strand-specific settings. Differential expression analysis was performed using edgeR v4.0.16 [65] with Trimmed Mean of M-values (TMM) normalization. Expression values were represented as log2[counts per million (CPM) + 1] for visualization and differentially expressed genes (DEGs) identified using a fold change cutoff of 1.5 were used for downstream functional annotation. Functional enrichment analysis of DEGs was performed using the Database for Annotation, Visualization and Integrated Discovery (DAVID) Bioinformatics Resources [66], including Gene Ontology Biological Process (GO-BP) and Kyoto Encyclopedia of Genes and Genomes (KEGG) pathway analyses.

2.12 Statistical analysis

All statistical analyses were performed using GraphPad Prism version 10 (GraphPad Software, California, USA). Data are presented as mean ± standard deviation (SD). Statistical significance was assessed using unpaired t-tests, one-way or two-way analysis of variance (ANOVA), or mixed-effects analysis, as appropriate, followed by Dunnett's or Tukey's multiple-comparison tests. Significance thresholds were defined as follows: $^{*}P < 0.05$; $^{**}P < 0.01$; $^{***}P < 0.001$; ns = not significant. Each experiment was conducted using a minimum of three independent biological replicates.

3 Results

3.1 Fabrication of the NICHE-chip for geometry-controlled neurosphere culture and ISF-like flow regulation

A platform containing microwells with matched diameters and depths was fabricated to control hNSC neurosphere geometry within a single batch using a 3D printing-based molding technique. Initially, a mold was created using photocurable resin *via* DLP-based 3D printing, which was then replicated in PDMS to form the final platform. Prior to producing the final platform, printability and mechanical properties of specimens under various conditions were compared.

Typical dog-bone-shaped samples following the ISO-527-2 Type 5B design were fabricated under various DLP curing conditions to evaluate the suitability of the photocurable solution for NICHE-chip mold fabrication (Fig. S1A). The designed structures were reproduced under most conditions, and samples fabricated within the appropriate curing range of up to 6 s, showed sharp boundaries and uniform surface morphology (Fig. S1B). In contrast, excessive curing above 8 s caused broadened edges, surface deformation, and increased dimensional errors, with maximum deviations exceeding 50% (Fig. S1C). Tensile testing showed that all samples maintained structural integrity during deformation, while tensile resistance and stiffness improved with increasing curing time up to an intermediate range; however, excessive curing provided limited additional mechanical improvement and corresponded to overcuring-induced deformation (Fig. S2).

Considering the cylindrical geometry of the NICHE-chip mold, cylindrical structures were further fabricated under narrowed curing conditions of 2 s, 4 s, and 6 s (Fig. S3). Curing for 2 s resulted in incomplete polymerization and partial structural collapse, whereas curing for 4 and 6 s enabled the fabrication of cylindrical structures with smooth surfaces and clear boundaries, although partial overcuring was observed at 6 s (Fig. S3A). Quantitative analysis showed that structures cured for 4 s exhibited dimensional errors below 1%, whereas 2 s and 6 s resulted in larger deviations (Fig. S3B). Compression testing confirmed stable load-bearing behavior and sufficient compressive stability for NICHE-chip fabrication (Fig. S4). Based on the combined dimensional precision and mechanical properties, a curing time of 4 s was selected as the optimal condition.

Using the optimized printing condition, the 3D-printed mold was fabricated and then replicated in PDMS to produce the microwell-based platform. This platform included microwells with matched diameters and depths of 100, 250, and 400 μm. These variations allowed for the systematic investigation of how changes in both neurosphere geometry and microenvironmental factors influence hNSC behavior (Figs. 1 and S5).

Next, we designed a system to more closely mimic the low-velocity ISF flow observed in NSC niches. Given that physiologically relevant brain ISF flow has been reported in the range of 6 to 18 μL/h [14], we aimed to generate a low and stable flow rate that would remain within this range. To achieve this, we incorporated an osmotic pump at the outlet of the device, designed according to a previously reported protocol [52]. As illustrated in Fig. 1C, the tubing segment connected to the osmotic pump was filled with DI water, whereas the segment connected to the microfluidic device contained culture medium. Due to the formation of an air gap between the two fluid columns, the DI water and culture medium remained physically separated, preventing direct contact and convective mixing. As a result, dilution of the culture medium was negligible during operation, allowing stable medium flow within the device. Osmotic pressure generated across a semipermeable cellulose membrane separating DI water from an external PEG solution induced water efflux, creating negative pressure that drove medium flow through the microfluidic chip. This mechanism established continuous ISF-like flow while maintaining physical separation between the driving fluid and culture medium. Under a 0.5 M PEG condition, the internal weight of the reservoir cube increased by approximately 234 mg over the observation period, corresponding to an estimated average flow rate of approximately 14 μL/h (Fig. S6).

3.2 Size-controlled neurosphere formation and hNSC differentiation under NICHE-macro conditions

We first evaluated how size-controlled neurosphere formation in the multi-sized microwell chip influenced hNSC self-renewal and differentiation under static culture conditions. Typically, hNSCs maintain their self-renewal capacity in conventional two-dimensional (2D) culture plates when exposed to mitogens, such as bFGF and EGF, and undergo spontaneous differentiation into neuronal and glial lineages upon mitogen removal [31, 67]. In our experiment, hNSCs were maintained under self-renewal conditions for the first 2 days, followed by simple mitogen withdrawal to induce spontaneous differentiation. To assess the effect of the chip-defined microwell geometry independent of applied flow, hNSCs were cultured in the multi-sized microwell chip placed in a conventional culture dish without external flow, a condition designated as NICHE-macro. The differentiation capacity of hNSCs cultured under the NICHE-macro condition was compared with that of the control group (CTR) cultured in a conventional 2D culture plate (Fig. 2A).

To achieve uniform and compact neurosphere formation, the surface of the PDMS microwell chip was coated with HGC solution, based on a previously reported method [53]. Because PDMS can adsorb serum proteins and promote cell attachment, which may interfere with uniform aggregate formation [59], the microwell surface was modified with HGC. HGC has been reported to form a polymer-based ultra-low attachment (ULA) layer that suppresses cell–substrate adhesion and promotes compact aggregate formation through cell–cell aggregation [53, 68, 69]. Therefore, in this study, HGC coating was applied to minimize cell attachment within the PDMS microwells and facilitate the formation of uniform and compact neurospheres.

First, HGC was applied to the PDMS microwells according to a previously reported coating protocol [53]. The formation and surface characteristics of the HGC coating on the microwell platform were then evaluated. Cross-sectional SEM analysis confirmed the formation of an HGC coating layer on the PDMS microwell surface while preserving the original well geometry (Fig. S7A). Contact angle analysis showed that HGC coating reduced the water contact angle from approximately 100° to 71° (Fig. S7B), consistent with successful surface modification and previously reported values for HGC-coated surfaces [53]. In addition, attenuated total reflectance–Fourier transform infrared (ATR-FTIR) analysis showed characteristic HGC-related peaks in HGC-coated PDMS, including OH stretching around 3413 cm^{-1}, C–H stretching around 2962 cm^{-1}, and C=O stretching around 1643 cm^{-1} (Fig. S7C). These results demonstrate the presence of HGC-associated chemical functional groups on the

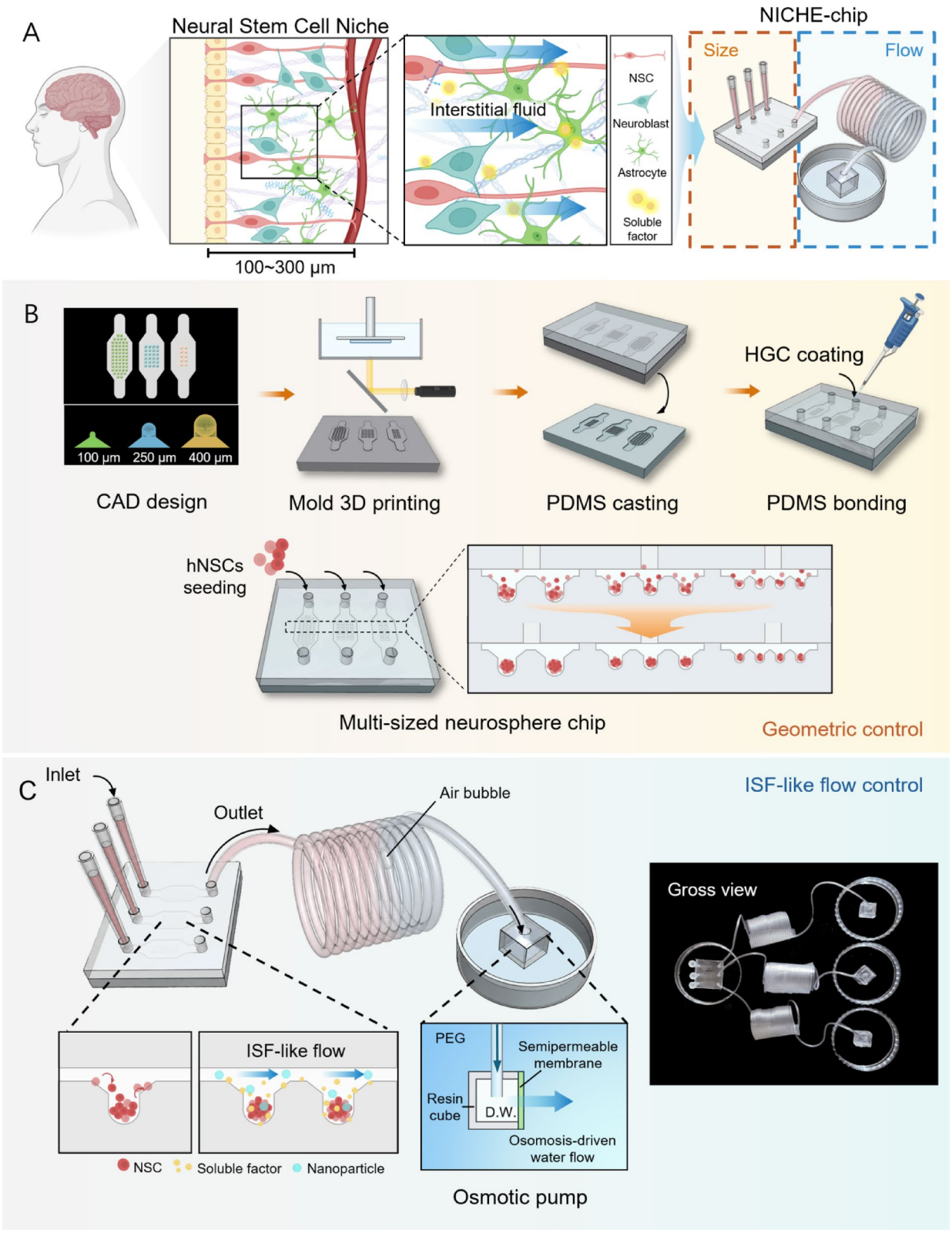

Fig. 1 NICHE-chip for generating size-controlled hNSC neurospheres in a single batch with integrated osmosis-driven ISF-like flow. **A** Schematic illustration of the NSC niche and its in vitro recapitulation using the NICHE-chip. The illustration was created using BioRender. **B** Fabrication workflow of the multi-sized neurosphere chip using a one-step 3D-printed mold. The chip contains arrays of microwells with systematically varied diameters and depths (100, 250, and 400 μm), enabling the generation of size-controlled hNSC neurospheres. **C** Integration of the microfluidic chip with an osmosis-driven pumping module to generate continuous ISF-like flow for soluble factor transport and nanoparticle-based delivery

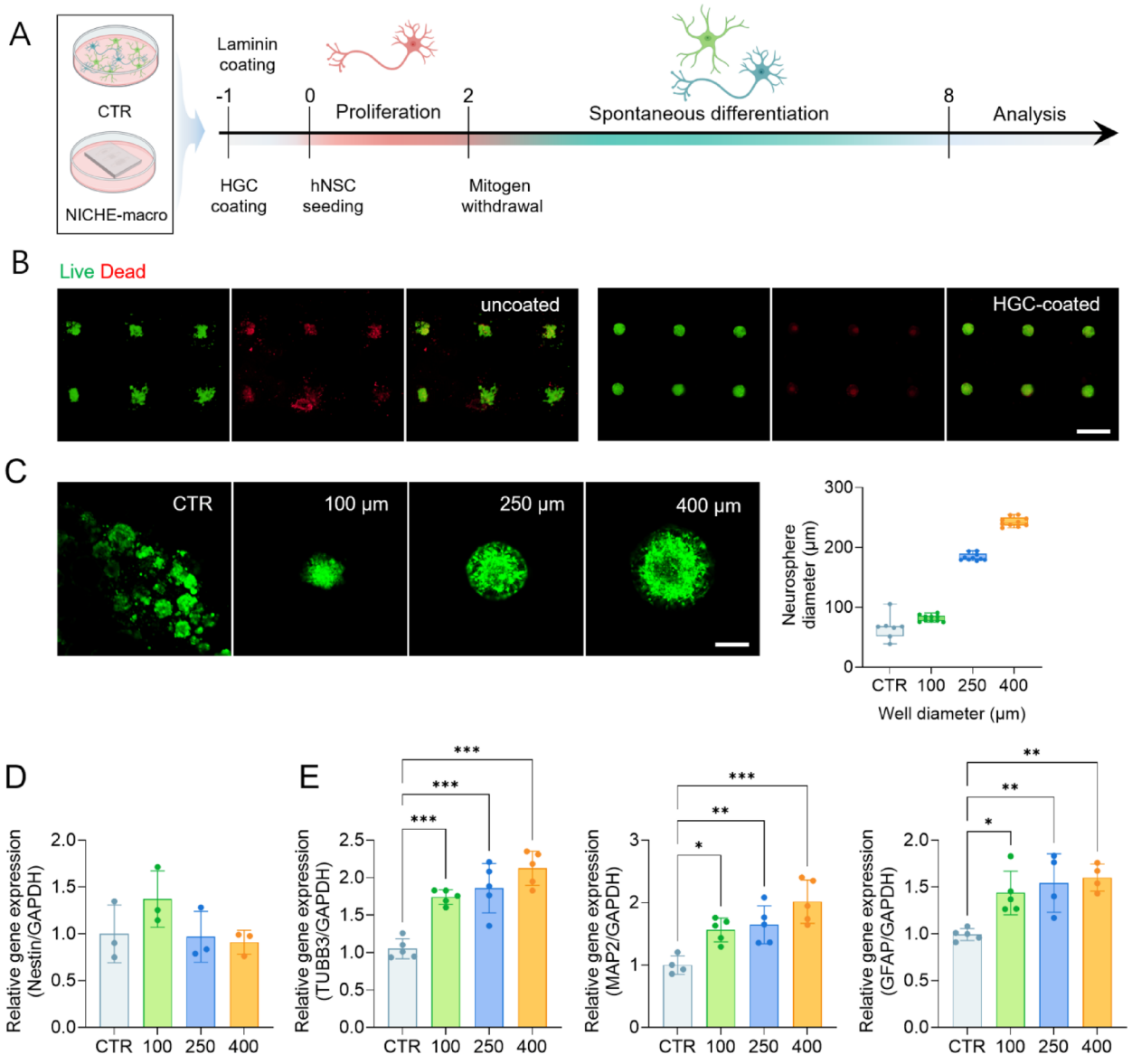

Fig. 2 Size-controlled hNSC neurosphere formation and regulation of hNSC self-renewal and differentiation in the multi-sized microwell chip. **A** Schematic workflow of hNSC culture and spontaneous differentiation under conventional 2D culture plate control (CTR) and NICHE-macro conditions (NICHE-macro: microwell chip placed in a conventional culture dish). The illustration was created using BioRender. **B** Representative live/dead fluorescence images of hNSCs cultured in uncoated and HGC-coated microwells, showing the effect of HGC coating on compact neurosphere formation. Scale bar = 500 μm. **C** Representative fluorescence images of Calcein AM-stained hNSC neurospheres formed in size-varied microwells, with quantification of neurosphere diameter distributions. Scale bar = 100 μm. **D** Quantification of relative *Nestin* gene expression at day 2 by qRT-PCR. **E** Quantification of relative *TUBB3*, *MAP2*, and *GFAP* gene expression at day 8 by qRT-PCR. Data are presented as mean ± SD; $n = 3–5$; *$P < 0.05$; **$P < 0.01$; ***$P < 0.001$ vs. CTR

PDMS surface and, together with the SEM and contact angle results, support the successful formation of an HGC coating layer on the PDMS microwell surface.

Based on this confirmed surface modification, HGC-coated PDMS microwells were subsequently used for hNSC culture. After 24 h of culture in the NICHE-macro chip, hNSCs in the uncoated chip showed limited aggregation and increased cell death, whereas stable neurosphere formation was observed in the HGC-coated microwells. These findings suggest that HGC-mediated surface modification may support 3D self-assembly, highlighting its importance in stable neurosphere formation within the chip (Figs. 2B and S8). Neurosphere formation was successfully observed in all microwell sizes, including microwells with matched diameters and depths of 100, 250, and 400 μm, indicating that the microwell design effectively facilitated 3D aggregation of hNSCs (Figs. 2C and S9). Moreover, neurospheres formed in the microwells exhibited uniform size distributions (Fig. 2C), and upon retrieval, they maintained consistent size and

sphericity, supporting the stability of the self-assembled structures (Fig. S8).

To assess the effect of geometric control on hNSC behavior, we quantified the expression of the self-renewal marker *Nestin*, neuronal markers *TUBB3* and *MAP2*, and the astrocytic marker *GFAP* across different microwell sizes and the conventional 2D culture plate control (CTR) using qRT-PCR. Differentiation into neuronal and glial lineages was induced by removing mitogens from the culture medium for an additional 6 days. No statistically significant differences in *Nestin* expression were observed among neurospheres of different sizes or between neurosphere and 2D culture conditions (Fig. 2D). In contrast, relative gene expression analysis revealed increased expression levels of differentiation markers, including *TUBB3*, *MAP2*, and *GFAP*, in neurospheres cultured in the multi-sized microwell chip compared with those cultured in conventional 2D plates (Fig. 2E). In particular, in the 100 μm neurosphere condition, *TUBB3* expression was 1.74-fold higher, *MAP2* expression was 1.56-fold higher, and *GFAP* expression was 1.44-fold higher than in the 2D culture condition, indicating enhanced neuronal and glial differentiation in neurospheres. The expression levels of these differentiation markers did not show statistically significant differences among neurospheres generated in 100, 250, and 400 μm microwells. These results suggest that chip-defined 3D neurosphere culture provides a favorable microenvironment for hNSC differentiation compared with conventional 2D culture, potentially through enhanced 3D cell–cell interactions and geometric confinement.

3.3 Impact of ISF-like flow on hNSC neurosphere self-renewal and differentiation in a confined 3D microenvironment

Our results showed that 3D culture provides a more favorable environment for hNSC differentiation than conventional 2D culture. However, no significant differences were observed according to neurosphere size. This may be because the culture system was still based on a macro-scale environment that differs from in vivo conditions. In vivo, cellular behavior is regulated not only by cell–cell interactions but also by various soluble factors, including mitogens and other paracrine factors, that are maintained within the local microenvironment [1]. Additionally, in such an environment, slow ISF flow plays a critical role in mass transport and the distribution of soluble factors within brain tissue [13]. Moreover, fluid flow can act as a signaling cue that regulates cellular behaviors such as cell–cell junction formation and ECM production [70–72]. However, in conventional macro-scale culture systems, these soluble factors can rapidly diffuse into the bulk medium, making it difficult to recapitulate in vivo-like conditions [73]. Therefore, we sought to investigate whether hNSC neurospheres exhibit size-dependent differences in hNSC behavior in an ISF-integrated 3D microenvironment.

To distinguish the effect of chip-defined confinement and ISF-like flow, we compared hNSC neurospheres under three NICHE-chip configurations: NICHE-macro, NICHE-static, and NICHE-ISF. As defined above, NICHE-macro refers to the multi-sized microwell chip placed in a conventional culture dish without external flow. NICHE-static refers to the assembled microfluidic chip with a 100 μm-high confined flow space but without applied flow, whereas NICHE-ISF refers to the same confined microfluidic chip operated with osmosis-driven ISF-like flow. As a preliminary experiment, we evaluated the effect of dynamic culture on neurosphere viability using a rocker-based system and observed enhanced neurosphere survival under dynamic conditions compared with static culture (Fig. S10). However, rocker-based culture generates bulk oscillatory flow and does not allow precise control of low-rate, confined ISF-like transport. Therefore, based on the beneficial effect of dynamic culture, we implemented continuous osmosis-driven ISF-like flow in our platform. The system was designed with a 100 μm-high flow space formed by sealing a top PDMS layer onto a bottom layer containing microwells with matched diameters and depths of 100, 250, and 400 μm, creating a confined 3D microenvironment. Using the osmotic pumping system, a controlled low-rate flow was generated to mimic physiologically relevant ISF-like flow conditions (Fig. 3A). After 6 days of differentiation, immunofluorescence staining revealed qualitatively higher GFAP and MAP2 signals in hNSCs cultured under the NICHE-ISF condition than in those cultured under the NICHE-static condition or the NICHE-macro condition (Fig. 3A, B).

To determine whether the enhanced differentiation marker expression was associated with altered self-renewal capacity before differentiation, *Nestin* expression was assessed on day 2 before inducing differentiation. The relative gene expression of *Nestin* was higher under the NICHE-ISF condition than under the NICHE-macro and NICHE-static conditions, with statistically significant upregulation observed particularly in the 100 μm group (Fig. 3C). In contrast, neurospheres generated in 250 μm and 400 μm microwells showed no statistically significant differences. This may be associated with more efficient delivery of mitogens, such as bFGF and EGF, within smaller neurospheres, as nutrient and growth factor diffusion is known to decrease with increasing neurosphere size. These findings are consistent with previous studies [74].

Quantitative analysis of differentiation-related gene expression also confirmed that neurospheres cultured under the NICHE-ISF condition exhibited higher

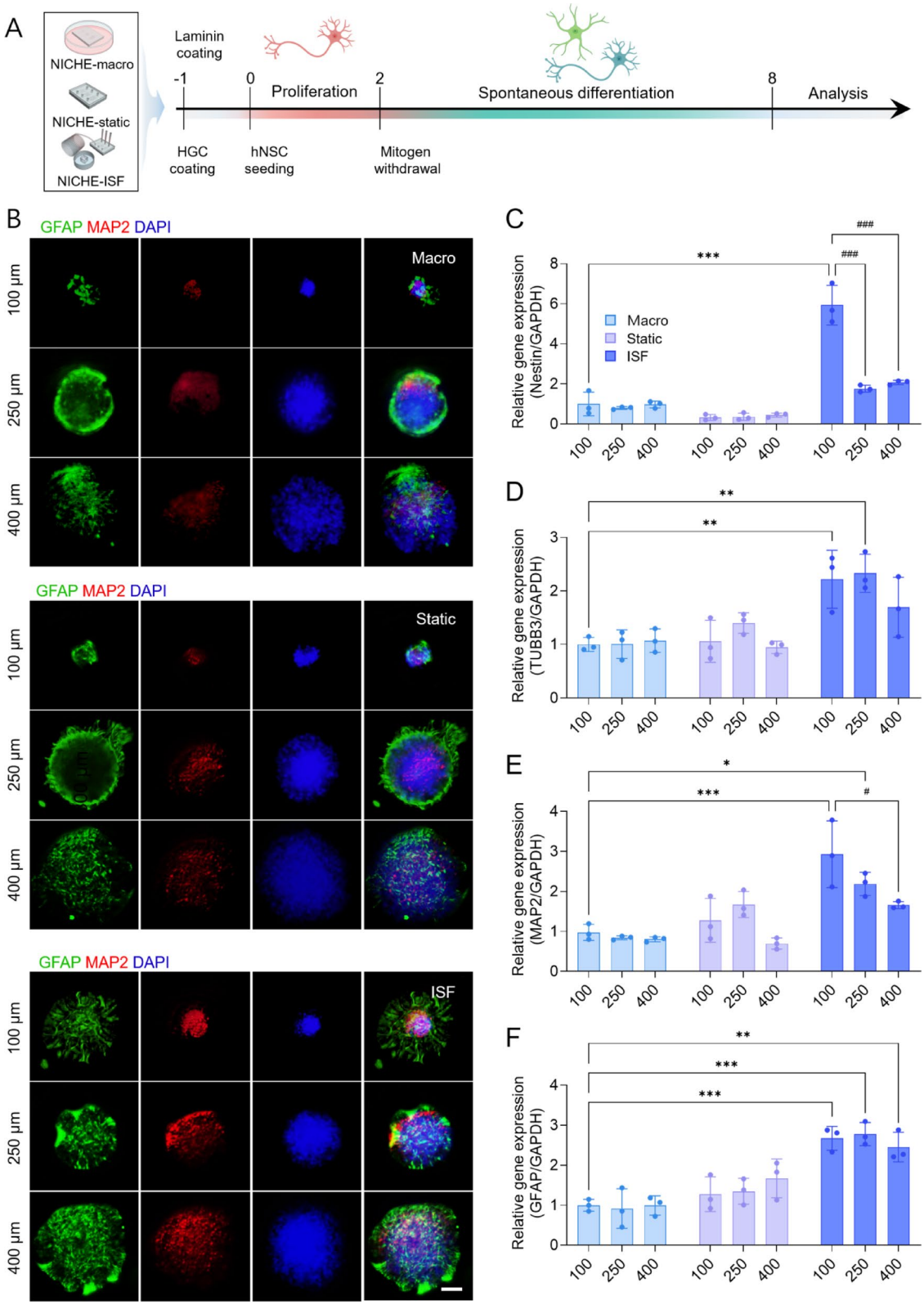

Fig. 3 (See legend on next page.)

(See figure on previous page.)

Fig. 3 Self-renewal and differentiation profiles of hNSC neurospheres under NICHE-macro, NICHE-static, and NICHE-ISF conditions. **A** Schematic workflow of hNSC culture and spontaneous differentiation under NICHE-macro, NICHE-static, and NICHE-ISF conditions (NICHE-macro: microwell chip placed in a conventional culture dish; NICHE-static: assembled chip without flow; NICHE-ISF: assembled chip with osmosis-driven ISF-like flow). **B** Representative immunofluorescence images of hNSC neurospheres after 6 days of differentiation, stained for GFAP (green), MAP2 (red), and DAPI (blue). Scale bar = 100 μm. **C** Quantification of relative *Nestin* gene expression at day 2 by qRT-PCR. **D**–**F** Quantification of relative *TUBB3*, *MAP2*, and *GFAP* gene expression at day 8 by qRT-PCR. ($n = 3$; $^{*}P < 0.05$; $^{**}P < 0.01$; $^{***}P < 0.001$ vs. 100 μm NICHE-macro, $^{\#}P < 0.05$; $^{\#\#\#}P < 0.001$ vs. 100 μm NICHE-ISF)

expression of differentiation markers. Both neuronal markers, *TUBB3* and *MAP2*, and the astrocytic marker *GFAP* showed significantly increased expression under the NICHE-ISF condition compared with the NICHE-macro and NICHE-static conditions. In particular, the increase relative to NICHE-static suggests that ISF-like flow may contribute additional effects beyond those associated with geometric confinement alone. In addition, analysis of size-dependent effects revealed that neurospheres with different sizes did not exhibit significant size-dependent differentiation patterns under NICHE-macro or NICHE-static conditions. However, under the NICHE-ISF condition, 100 μm neurospheres showed notably higher neuronal differentiation marker expression compared with larger neurospheres. The stronger response observed in 100 μm neurospheres may reflect the combined effects of neurosphere geometry, enhanced local transport, and size-dependent cell–cell and cell–ECM interactions under NICHE-ISF conditions.

3.4 Potential mechanisms underlying enhanced hNSC survival and differentiation under NICHE-ISF conditions

To assess the contribution of ISF-like flow to local mass transport within the same confined microenvironment, we simulated EGF and bFGF transport under NICHE-static and NICHE-ISF conditions (Fig. S11). EGF and bFGF reached a near-uniform distribution within 15 min under NICHE-ISF conditions, whereas more than 10 h was required under NICHE-static conditions.

Based on these observations, we next investigated whether the enhanced self-renewal and differentiation observed under NICHE-ISF conditions were associated with improved cell survival and strengthened cell–cell and cell–ECM interactions. To this end, we first analyzed cell viability and apoptosis in neurospheres cultured under NICHE-static and NICHE-ISF conditions (Fig. 4A). After 2 days of culture, cell viability was assessed using live/dead staining, and apoptosis-related gene expression was analyzed by qRT-PCR. A significantly lower proportion of dead cells was observed in the NICHE-ISF group than in the NICHE-static group (Fig. 4B). Furthermore, relative gene expression levels of the pro-apoptotic marker *BAX* and the anti-apoptotic marker *BCL2* were analyzed, indicating a higher apoptosis-related index in the NICHE-static group than in the NICHE-ISF group (Fig. 4C). These results suggest that ISF-like flow improves hNSC viability and survival within the confined 3D microenvironment, thereby providing a supportive condition for subsequent self-renewal and differentiation responses.

Building on previous studies suggesting that ISF-like flow can enhance cell–cell and cell–ECM interactions during spheroid formation, we analyzed how ISF-like flow in the microenvironment impacts these interactions in hNSCs. Recent research suggests that the interaction between hNSCs and ECM proteins promotes self-renewal and neuronal differentiation [75]. Given that, we expected that neurospheres cultured under NICHE-ISF conditions would express higher levels of laminin, a key ECM component of NSC niches. To investigate this, we compared laminin fluorescence intensity and gene expression in neurospheres cultured under NICHE-static and NICHE-ISF conditions using immunofluorescence and qRT-PCR assays, respectively. Based on the pronounced cellular responses observed in 100 μm neurospheres under NICHE-ISF conditions, this condition was selected for further analysis. Immunofluorescence staining revealed stronger laminin signals, particularly toward the inner regions of hNSC neurospheres under NICHE-ISF conditions compared with NICHE-static conditions (Fig. 4D). Consistently, quantitative analysis showed significantly higher relative laminin fluorescence intensity under NICHE-ISF conditions (Fig. 4E). qRT-PCR analysis further confirmed that *Laminin* expression was significantly elevated in neurospheres cultured under ISF-like flow conditions. In addition to ECM expression, *CDH2* expression was also higher in the flow-cultured neurospheres than in those cultured under static conditions (Fig. 4F, G). These findings suggest that cell–cell and cell–ECM interactions may contribute to the enhanced differentiation of hNSCs, and that the degree of these interactions can be influenced by ISF-like flow.

3.5 Aβ-induced AD-like neurotoxicity modeling and nanoparticle-mediated BDNF neuroprotection in the ISF-integrated NICHE-chip

Having established that the NICHE-ISF condition enhances hNSC survival, self-renewal, differentiation, and cell–matrix interactions, we next examined whether this validated microenvironment could be applied to disease-relevant neurotoxicity modeling. Among the tested conditions, 100 μm neurospheres cultured under NICHE-ISF conditions showed relatively robust ISF-responsive cellular responses; therefore, this condition

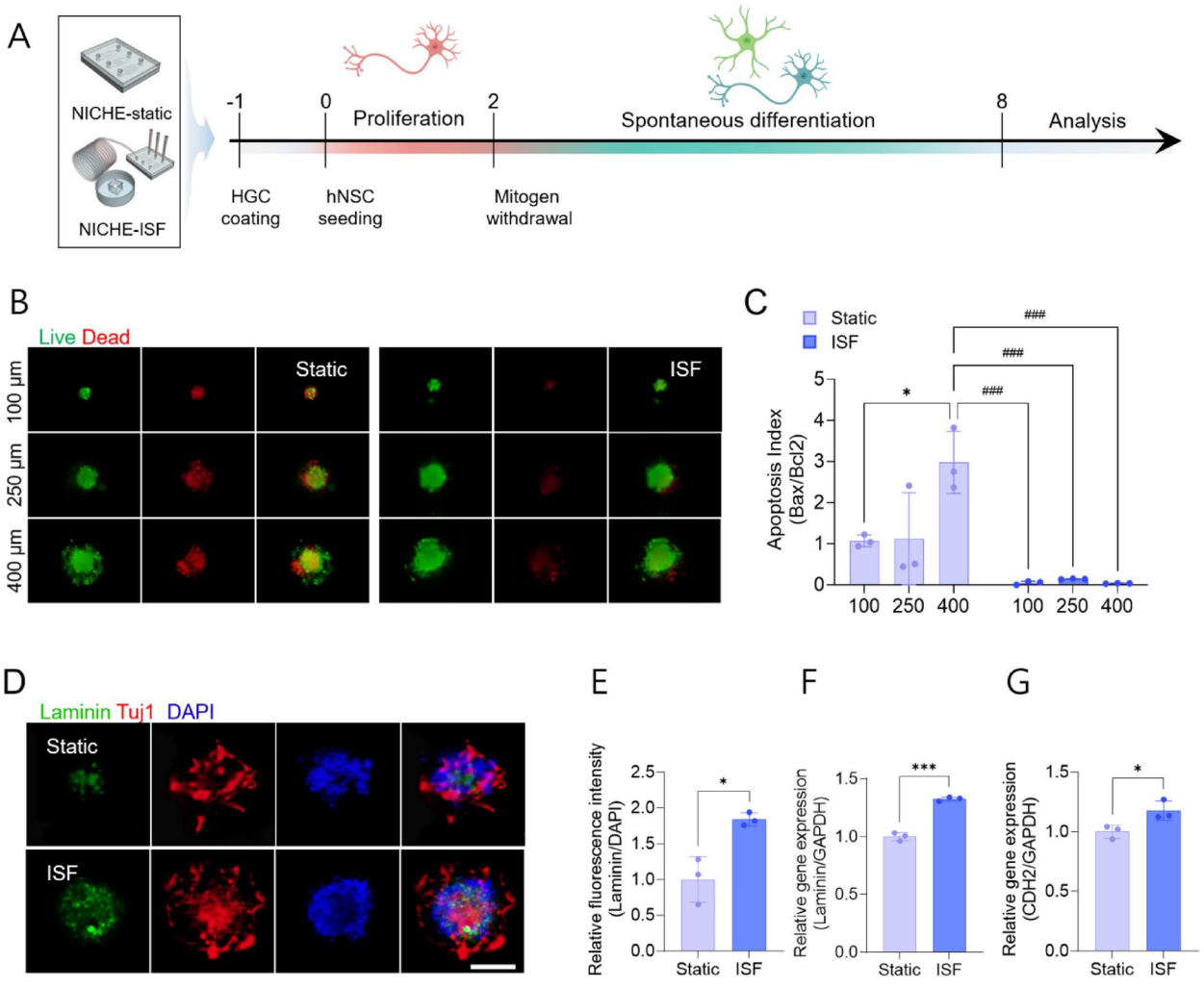

Fig. 4 ISF-like flow-mediated enhancement of hNSC neurosphere survival, ECM production, and cell–cell interactions in the 3D NICHE-chip microenvironment. **A** Schematic overview of hNSC neurosphere culture and spontaneous differentiation under NICHE-static and NICHE-ISF conditions. **B** Live/dead staining of hNSC neurospheres cultured under NICHE-static or NICHE-ISF conditions at day 2. Scale bar = 200 μm. **C** Apoptosis-related index quantified as the relative gene expression of *BAX*/*BCL2* by qRT-PCR at day 2 ($n = 3$; $^{*}P < 0.05$ vs. 100 μm NICHE-static, $^{\#\#\#}P < 0.001$ vs. 400 μm NICHE-static). **D** Representative laminin and Tuj1 immunostaining images of hNSC neurospheres formed in 100 μm microwells at day 8 under NICHE-static or NICHE-ISF conditions. Scale bar = 100 μm. **E** Relative laminin fluorescence intensity of hNSC neurospheres, normalized to DAPI signal. **F**, **G** Quantification of relative gene expression of *Laminin* and *CDH2* at day 8 by qRT-PCR ($n = 3$; $^{*}P < 0.05$; $^{***}P < 0.001$ vs. 100 μm NICHE-static)

was selected for subsequent Aβ-induced AD-like neurotoxicity modeling. Aβ accumulation is a major pathological feature of AD and is known to induce neuronal cell death and neurodegeneration [76]. We introduced Aβ into the platform to model AD-related neurotoxicity under an ISF-like flow microenvironment. Consistent with the previous results, simulation of oligomeric Aβ transport confirmed more efficient delivery under NICHE-ISF than under NICHE-static conditions (Fig. S11). Simultaneously, BDNF, a neurotrophin primarily expressed in neurons and glial cells and known to exert neuroprotective effects [46–48], was selected as a representative neuroprotective factor because of its established relevance in Aβ-induced neurotoxicity models. Aβ has been reported to suppress the production of BDNF [58], and reduced BDNF levels have been observed in patients with Alzheimer's disease [77]. Furthermore, BDNF treatment has been shown to ameliorate neurotoxicity and cognitive impairment in AD models [46]. Given its therapeutic relevance, an Aβ and BDNF-NP group was included to evaluate potential neuroprotective effects. We hypothesized that continuous low-rate flow would facilitate sustained Aβ exposure while providing a controlled microenvironment for evaluating BDNF-NP-mediated neuroprotection.

However, soluble BDNF has a short biological half-life and may undergo rapid degradation under physiological conditions [48–50], limiting its ability to maintain sustained local neurotrophic support. Therefore, to more stably evaluate BDNF-mediated neuroprotection in the

NICHE-chip, we further introduced BDNF-NPs as a sustained-release delivery system. PLGA-based delivery systems are widely used biodegradable and biocompatible platforms for the controlled release of proteins and growth factors [78, 79] and have also been applied to sustained BDNF delivery [50]. Based on this rationale, we aimed to evaluate AD-like neurotoxicity and BDNF-NP-mediated neuroprotection by comparing untreated control, Aβ-only, and Aβ + BDNF-NP treatment groups under NICHE-static and NICHE-ISF conditions (Fig. 5A, B).

BDNF-NPs were fabricated based on a previously reported protocol [59]. SEM analysis showed that the fabricated BDNF-NPs exhibited spherical morphology and nanoscale dimensions (Fig. 5C). Particle size distribution analysis revealed that the PLGA nanoparticles were mainly distributed within the 201–400 nm range, with the highest fraction observed in the 201–300 nm range (Fig. 5D). These results indicate that the fabricated PLGA nanoparticles formed a nanoscale population suitable for use as BDNF delivery carriers. Release profile analysis showed that BDNF-NPs exhibited a relatively rapid initial burst release during the first day, with approximately 51.0% of BDNF released by day 1 (Fig. 5E). Thereafter, the release rate gradually decreased, but sustained release was maintained, reaching approximately 80% cumulative release by day 7. These results suggest that BDNF-NPs can provide sustained BDNF release after the initial burst phase, supporting their use for prolonged neurotrophic factor delivery in subsequent NICHE-chip experiments. Considering the release profile and encapsulation efficiency, the BDNF loading amount was adjusted to achieve a final treatment concentration of 20 ng/mL, and this formulation was used in subsequent experiments.

To induce neurotoxicity in differentiated neural populations, hNSC neurospheres were allowed to undergo spontaneous differentiation for 3 days, followed by treatment with 5 μM Aβ alone or 5 μM Aβ combined with BDNF-NPs, adjusted to provide an equivalent BDNF concentration of 20 ng/mL, for an additional 3 days (Fig. 5A, B). Aβ was prepared as soluble oligomers following a previously reported protocol [57]. Immunofluorescence analysis showed that under static conditions, neuronal and astrocytic marker signals were relatively weak. In contrast, under ISF-like flow conditions, both markers exhibited markedly stronger fluorescence intensity and more distinct cellular morphology, with Tuj1 fluorescence intensity in the control group increasing by approximately 3-fold compared to static culture in untreated control (NICHE-static vs. NICHE-ISF) (Fig. 5F, G). Consistent with previous reports [80], Aβ treatment did not induce a noticeable change in astrocyte abundance across any of the experimental groups (Fig. 5F, H). In contrast, neuronal responses varied depending on Aβ and BDNF-NP treatment. Exposure to 5 μM Aβ resulted in a reduction of Tuj1 fluorescence intensity under both static and NICHE-ISF conditions. Compared with their control groups, Tuj1 fluorescence intensity decreased to approximately 42% under static conditions and to about 25% under NICHE-ISF conditions, with statistical significance observed only in the NICHE-ISF group (Fig. 5G). Co-treatment with BDNF-NPs mitigated Aβ-induced neurotoxicity in both culture conditions. In the static group, Tuj1 fluorescence intensity increased by approximately 2.17-fold compared to the Aβ-only group, although this change was not statistically significant. In contrast, the NICHE-ISF group showed a significant 4.17-fold increase relative to the Aβ-only group (Fig. 5G). These results suggest that continuous ISF-like flow in the NICHE-chip platform supports Aβ-induced AD-like neurotoxicity modeling under continuous ISF-like transport and provides a useful framework for evaluating BDNF-NP-mediated neuroprotection.

3.6 Transcriptomic analysis of BDNF-NP-mediated neuroprotection in the ISF-integrated AD-like model

To investigate the transcriptional features underlying Aβ-induced neurotoxicity and BDNF-NP-mediated neuroprotection, RNA sequencing was performed on three experimental groups: untreated control (CTR), Aβ-treated, and Aβ + BDNF-NP-treated groups (Aβ + BDNF-NP) (Fig. 6A). To examine whether BDNF-NP treatment could transcriptionally counteract Aβ-induced neurotoxicity, DEGs from two comparisons, Aβ vs. CTR and Aβ + BDNF-NP vs. Aβ, were intersected using Venn diagram analysis. This analysis identified 181 oppositely regulated genes that showed inverse regulatory patterns between the two comparisons (Fig. 6B). These genes were upregulated or downregulated by Aβ treatment and showed opposite-direction changes upon BDNF-NP treatment, suggesting partial counter-regulation of Aβ-induced transcriptional alterations. Heatmap analysis further showed that, among the 181 oppositely regulated genes, the Aβ group displayed a distinct expression pattern, whereas the Aβ + BDNF-NP group showed a partial shift toward the CTR pattern (Fig. 6C).

To further characterize the transcriptional programs associated with Aβ-induced neurotoxicity and BDNF-NP-mediated neuroprotection, we examined representative gene sets related to apoptosis, stress responses, cytoskeletal regulation, and synaptic plasticity, all of which are implicated in Aβ-mediated neurotoxicity [81–84] (Fig. 6D). Across these categories, representative genes showed opposite regulatory patterns between the Aβ vs. CTR and Aβ + BDNF-NP vs. Aβ comparisons. In the apoptosis-associated gene set, pro-survival or anti-apoptotic genes, including *BIRC5* and *BCL2L12*, were downregulated by Aβ and shifted in the opposite

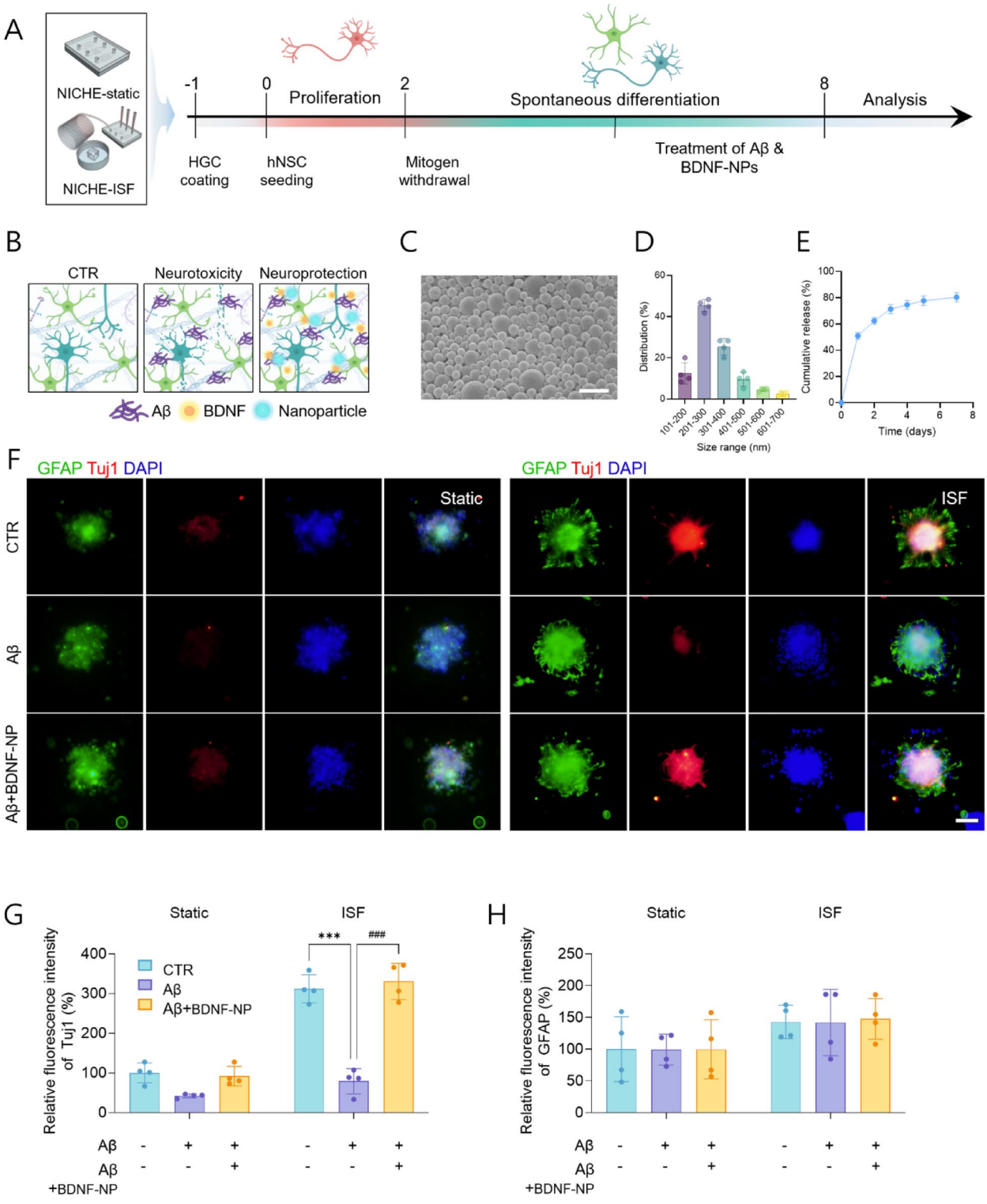

Fig. 5 Aβ-induced AD-like neurotoxicity modeling and BDNF-NP-mediated neuroprotection in the ISF-integrated NICHE-chip. **A** Schematic workflow of Aβ-induced neurotoxicity modeling and BDNF-NP-mediated neuroprotection in the 3D NICHE-chip under NICHE-static and NICHE-ISF conditions. **B** Schematic representation of the experimental model for Aβ-induced neurotoxicity and BDNF-NP-mediated neuroprotection. **C** Representative scanning electron microscopy (SEM) image of the fabricated BDNF-NPs. Scale bar = 1 μm. **D** Size distribution of BDNF-NPs quantified from SEM images. **E** Cumulative BDNF release profile from BDNF-NPs over 7 days. **F** Representative immunofluorescence images of hNSC neurospheres stained for GFAP, Tuj1, and DAPI under untreated control (CTR), Aβ-treated, and Aβ + BDNF-NP-treated conditions. Scale bar = 100 μm. **G**, **H** Relative fluorescence intensity of Tuj1 and GFAP in hNSC neurospheres under NICHE-static and NICHE-ISF conditions. Data are presented as mean ± SD; $n = 4$. Statistical comparisons are indicated by brackets; $^{***}P < 0.001$; $^{\#\#\#}P < 0.001$

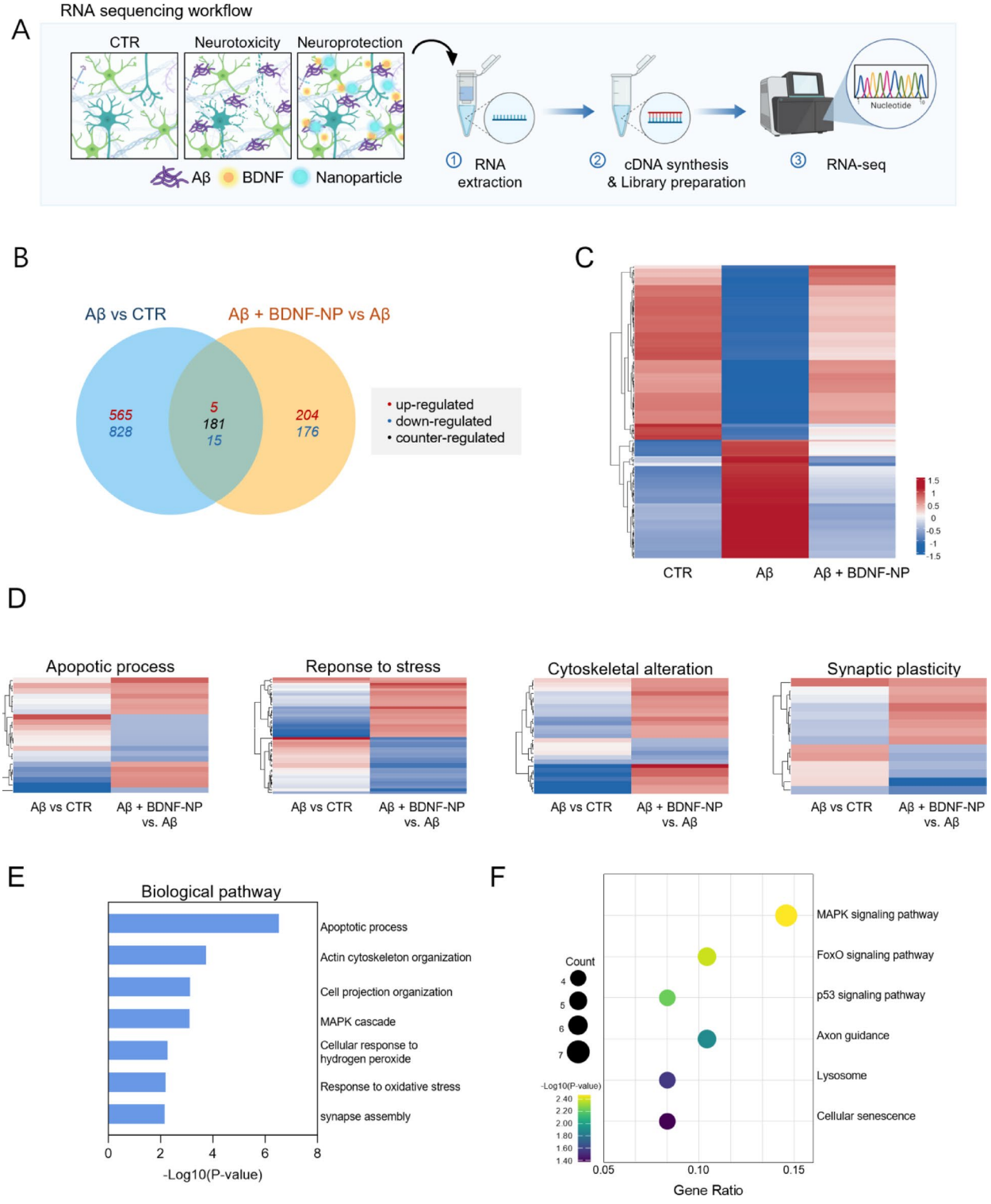

Fig. 6 Transcriptomic analysis of Aβ-induced transcriptional alterations and BDNF-NP-mediated counter-regulation. **A** Schematic overview of the RNA sequencing workflow for the untreated control (CTR), Aβ-induced neurotoxicity, and Aβ + BDNF-NP groups. **B** Venn diagram of DEGs identified in the Aβ vs. CTR and Aβ + BDNF-NP vs. Aβ comparisons. Red, blue, and green numbers indicate upregulated, downregulated, and oppositely regulated genes, respectively. **C** Heatmap of the 181 oppositely regulated genes across the CTR, Aβ, and Aβ + BDNF-NP groups. **D** Heatmaps of selected functional gene sets related to apoptotic process, response to stress, microtubule-based process, and synaptic plasticity in the Aβ vs. CTR and Aβ + BDNF-NP vs. Aβ comparisons. **E** GO-BP enrichment analysis of DEGs identified in the Aβ + BDNF-NP vs. Aβ comparison. **F** KEGG pathway enrichment analysis of DEGs identified in the Aβ + BDNF-NP vs. Aβ comparison

direction following BDNF-NP treatment, whereas stress- or apoptosis-associated genes such as *CHAC1* showed the reverse pattern [85–87]. Stress response-related genes also showed BDNF-NP-associated counter-regulation, including *TFEB*, a regulator of lysosomal biogenesis and autophagy that has been associated with Aβ clearance and proteostasis in AD-related contexts [88]. In addition, genes associated with cytoskeletal regulation and synaptic function, including *LIMK2*, *DLG3*, and *SYNGR1*, were modulated in opposite directions by Aβ and BDNF-NP treatment. These processes are closely linked to Aβ-associated cytoskeletal dysfunction, synaptic impairment, and neuronal degeneration [83, 89–92]. These results suggest that BDNF-NP treatment counter-regulates multiple Aβ-affected transcriptional programs related to cell survival, stress response, cytoskeletal organization, and synaptic function.

Consistent with these heatmap findings, GO-BP enrichment analysis of DEGs from the Aβ + BDNF-NP vs. Aβ comparison showed significant enrichment of terms related to apoptotic process, actin cytoskeleton organization, cell projection organization, mitogen-activated protein kinase (MAPK) cascade, oxidative stress response, and synapse assembly (Fig. 6E). KEGG pathway analysis further revealed enrichment of MAPK signaling, Forkhead box O (FoxO) signaling, p53 signaling, axon guidance, lysosome, and cellular senescence pathways (Fig. 6F). These enriched pathways are broadly associated with neuronal survival, apoptosis regulation, oxidative stress response, cytoskeletal remodeling, synaptic organization, and proteostasis [93–97]. Notably, enrichment of MAPK signaling is consistent with the involvement of BDNF-tropomyosin receptor kinase B (TrkB) downstream signaling in neuronal survival [93].

Overall, these transcriptomic analyses suggest that Aβ treatment induces broad gene expression changes across multiple neurotoxicity-associated processes, whereas BDNF-NP treatment counter-regulates a subset of these alterations. These findings provide transcriptomic support for the neuroprotective effects of BDNF-NPs observed in the ISF-integrated NICHE-chip AD-like neurotoxicity model.

4 Discussion

NSCs reside within specialized brain niches that are essential for maintaining their unique functional properties [1]. Within these niches, 3D architecture and ISF-mediated microenvironmental regulation play important roles [2]. Although the field of biofabrication has sought to develop sophisticated in vitro models, platforms that simultaneously integrate multi-microwell systems with physiologically relevant ISF-like flow have remained limited. In this study, we aimed to recapitulate key elements of the NSC niche by employing a 3D printing-based multi-sized microwell platform to precisely control hNSC neurosphere geometry within a single device and by incorporating an osmotic pump to provide continuous ISF-like flow.

Reliable fabrication of the NICHE-chip required precise mold geometry and sufficient mechanical stability, as deformation during replica molding or repeated handling could reduce the reproducibility of microwell dimensions. The optimized curing condition therefore provided an important technical basis for generating geometrically consistent neurospheres and comparing geometry-dependent hNSC responses.

A key implication of this study is that ISF-like flow should be considered not merely as a perfusion strategy but as a dynamic microenvironmental regulator. ISF-like flow may influence hNSC behavior by regulating soluble factor transport, waste removal, local biochemical gradients, and potentially mechanotransduction-related signaling. Importantly, these effects were dependent on neurosphere geometry, suggesting that geometric confinement and ISF-like transport act together to shape NSC survival and differentiation.

Using this platform, we systematically evaluated the effects of neurosphere geometry and microenvironmental conditions on cellular behaviors, including cell viability, self-renewal, differentiation potential, ECM organization, and cell–cell interactions. Using the ISF-integrated 100 μm neurosphere condition to establish an AD-like neurotoxicity model, oligomeric Aβ transport simulations further showed more efficient delivery under NICHE-ISF than under NICHE-static conditions, supporting the ability of the platform to regulate disease-relevant molecular transport (Fig. S11). BDNF-NPs were then used to evaluate neuroprotective responses within the ISF-integrated microenvironment. In addition, transcriptomic analysis was performed to investigate transcriptional programs associated with Aβ-induced neurotoxicity and BDNF-NP-mediated neuroprotection. The results showed that BDNF-NP treatment counter-regulated a subset of Aβ-induced transcriptional alterations, suggesting coordinated neuroprotective modulation at the transcriptional level.

A key strength of this platform is its ability to reveal geometry-dependent responses to ISF-like flow, which have been difficult to systematically identify in previous ISF-integrated microfluidic systems based on single-sized wells [98]. These results show that the proposed platform can serve as a physiologically relevant in vitro model of the NSC niche and as a useful tool for neurodegenerative disease modeling and therapeutic evaluation.

Several additional analyses may further improve the mechanistic interpretability and disease relevance of this platform. Although the present simulations demonstrated flow-dependent differences in soluble factor

transport, the individual contributions of geometric confinement, local concentration gradients, residence time, and mechanotransduction were not fully resolved. Therefore, future studies should independently quantify these parameters to further dissect their respective contributions to hNSC responses. Furthermore, although neuronal responses were evaluated using Tuj1 and MAP2, additional mature neuronal and synaptic markers, such as Synapsin I, synaptophysin, and Postsynaptic density protein 95 (PSD-95), were not experimentally assessed in the present study. Analysis of these markers in future studies would provide further insight into whether the observed neuroprotective effects are associated with enhanced neuronal maturation and synapse-related responses. In addition, although this study was based on heterogeneous neural cell populations generated through spontaneous differentiation and thus reflects certain features of the native niche, the introduction of additional glial and immune-related cell populations may enable more precise disease modeling. For instance, co-culture systems including astrocytes and microglia may allow more physiologically relevant modeling of Aβ-induced toxicity and neuroinflammatory responses [99]. Overall, this platform recapitulates key features of the NSC niche by integrating precise geometric control with ISF-like flow dynamics and may be further developed as a scalable system for neurodegenerative disease modeling and drug response evaluation.

5 Conclusion

In this study, we established a culture platform integrating 3D printing-based multi-sized microwells with osmotic pump-driven ISF-like flow and systematically investigated its effects on the behavior of hNSC neurospheres. We found that neurosphere geometry influenced cell viability, expression of self-renewal and differentiation markers, ECM organization, and cell–cell interactions, with these effects being more pronounced under ISF-like flow conditions than under static culture. Notably, the ISF-like flow in relatively smaller wells consistently enhanced indicators of self-renewal and neural differentiation. Furthermore, in the ISF-integrated 100 μm neurosphere model , Aβ treatment enabled modeling of AD-like neurotoxic responses. To evaluate the platform for sustained therapeutic delivery, BDNF was encapsulated in biodegradable PLGA nanoparticles and applied to the Aβ-induced neurotoxicity model. Treatment with BDNF-NPs partially restored neuronal marker signals, as assessed by immunofluorescence analysis, and counter-regulated a subset of Aβ-induced transcriptional alterations. Together, these results demonstrate that physical parameters—namely geometric confinement and ISF-like flow conditions—play important roles in regulating hNSC behavior and modulating cellular responses to pathological stimuli within a 3D in vitro microenvironment.

Abbreviations

NSC	Neural stem cell
SVZ	Subventricular zone
ISF	Interstitial fluid
ECM	Extracellular matrix
bFGF	Basic fibroblast growth factor
EGF	Epidermal growth factor
AD	Alzheimer's disease
DMT	Disease-modifying therapy
3D	Three-dimensional
Aβ	Amyloid-β
NICHE	Neural-Inspired Culture for a Hydrodynamic Environment
DLP	Digital light processing
hNSC	Human neural stem cell
BDNF	Brain-derived neurotrophic factor
PLGA	Poly(lactic-co-glycolic acid)
BDNF-NP	BDNF-loaded poly(lactic-co-glycolic acid) nanoparticle
CAD	Computer-aided design
tBA	Tert-butyl acrylate
HDDA	1,6-hexanediol diacrylate
PDMS	Polydimethylsiloxane
PEG	Polyethylene glycol
DI	Deionized
DMEM/F-12	Dulbecco's Modified Eagle's Medium/Nutrient Mixture F-12
P/S	Penicillin–streptomycin
HGC	Hexanoyl glycol chitosan
DPBS	Dulbecco's phosphate-buffered saline
DMSO	Dimethyl sulfoxide
SEM	Scanning electron microscopy
ELISA	Enzyme-linked immunosorbent assay
BSA	Bovine serum albumin
MAP2	Microtubule-associated protein 2
GFAP	Glial fibrillary acidic protein
IgG	Immunoglobulin G
H + L	Heavy and light chains
DAPI	4′,6-diamidino-2-phenylindole
Tuj1	βIII-tubulin
qRT-PCR	Quantitative real-time polymerase chain reaction
cDNA	Complementary DNA
BAX	BCL2-associated X protein
BCL2	B-cell lymphoma 2
TUBB3	Tubulin beta 3 class III
GAPDH	Glyceraldehyde-3-phosphate dehydrogenase
GRCh38	Genome Reference Consortium Human Build 38
STAR	Spliced Transcripts Alignment to a Reference
TMM	Trimmed mean of M-values
CPM	Counts per million
DEG	Differentially expressed gene
DAVID	Database for Annotation, Visualization and Integrated Discovery
GO-BP	Gene Ontology Biological Process
KEGG	Kyoto Encyclopedia of Genes and Genomes
SD	Standard deviation
ANOVA	Analysis of variance
CTR	Control
2D	Two-dimensional
ULA	Ultra-low attachment
ATR-FTIR	Attenuated total reflectance–Fourier transform infrared spectroscopy
CDH2	Cadherin 2
BIRC5	Baculoviral IAP repeat containing 5
BCL2L12	BCL2 like 12
CHAC1	ChaC glutathione-specific gamma-glutamylcyclotransferase 1
TFEB	Transcription factor EB
LIMK2	LIM domain kinase 2
DLG3	Discs large MAGUK scaffold protein 3
SYNGR1	Synaptogyrin 1
MAPK	Mitogen-activated protein kinase

FoxO	Forkhead box O
TrkB	Tropomyosin receptor kinase B

Acknowledgements
The schematic illustrations in the figures were created using BioRender and Shapr3D.

Author contributions
S.S., Y.L., and H.L. contributed equally to this work. K.Y. and H.D.J. conceived and supervised the study. S.S. and Y.L. performed the experiments, analyzed the data, and drafted the manuscript. H.L. contributed to the design and fabrication of the 3D-printed mold and microfluidic device. K.M.H. provided materials and technical support. S.S., Y.L., H.L., H.D.J., and K.Y. contributed to data interpretation. All authors reviewed and approved the final manuscript.

Funding
This work was supported by the Nano & Material Technology Development Program through the National Research Foundation of Korea (NRF) funded by the Ministry of Science and ICT (MSIT) (RS-2026-25537604) and the NRF grants funded by the Korean government (NRF2022R1C1C1008610, RS-2025-02243019, and RS-2025-00513935); the Korean Fund for Regenerative Medicine (KFRM) (KFRM22A0105L1-11 and KFRM24A0105L1); and the Korea Institute of Marine Science & Technology Promotion (KIMST) funded by the Ministry of Oceans and Fisheries (RS-2026-25541458).

Data availability
The data supporting the findings of this study are included in the main article and its supplementary materials. Additional datasets generated and/or analyzed during the current study are available from the corresponding author upon reasonable request.

Declarations

Competing interests
The authors declare that they have no competing interests.

Author details
[1]Department of Bioengineering and Nano-Bioengineering, Incheon National University, Incheon 22012, Republic of Korea
[2]Research Institute of Intelligent Manufacturing & Materials Technology, Korea Institute of Industrial Technology, Incheon 21999, Republic of Korea
[3]Division of Materials Science and Engineering, Hanyang University, Seoul 04763, Republic of Korea
[4]Department of Materials Science and Engineering, Chungnam National University, Daejeon 34134, Republic of Korea
[5]Department of Polymer Science and Engineering, Chungnam National University, Daejeon 34134, Republic of Korea
[6]Division of Bioengineering, Incheon National University, Incheon 22012, Republic of Korea
[7]Research Center for Bio Materials & Process Development, Incheon National University, Incheon 22012, Republic of Korea

Received: 28 August 2026 / Accepted: 13 October 2026
Published online: 20 October 2026

References

1. L.C. Fuentealba, K. Obernier, A. Alvarez-Buylla, Adult neural stem cells bridge their niche. Cell Stem Cell **10**, 698 (2012). https://doi.org/10.1016/j.stem.2012.05.012
2. M.I. Alonso, A. Gato, Cerebrospinal fluid and neural stem cell niche control. Neural Regen. Res. **13**, 1546 (2018). https://doi.org/10.4103/1673-5374.237114
3. F. Doetsch, J.M. García-Verdugo, A. Alvarez-Buylla, Cellular composition and three-dimensional organization of the subventricular germinal zone in the adult mammalian brain. J. Neurosci. **17**, 5046 (1997). https://doi.org/10.1523/JNEUROSCI.17-13-05046.1997
4. A. Quiñones-Hinojosa, K. Chaichana, The human subventricular zone: a source of new cells and a potential source of brain tumors. Exp. Neurol. **205**, 313 (2007). https://doi.org/10.1016/j.expneurol.2007.03.016
5. Y. Lei, H. Han, F. Yuan, A. Javeed, Y. Zhao, The brain interstitial system: anatomy, modeling, in vivo measurement, and applications. Prog Neurobiol. **157**, 230 (2017). https://doi.org/10.1016/j.pneurobio.2015.12.007
6. J.M. Klostranec, D. Vucevic, K.D. Bhatia, H.G.J. Kortman, T. Krings, K.P. Murphy, K.G. terBrugge, D.J. Mikulis, Current concepts in intracranial interstitial fluid transport and the glymphatic system: part I—anatomy and physiology. Radiology **301**, 502 (2021). https://doi.org/10.1148/radiol.2021202043
7. S.B. Hladky, M.A. Barrand, Mechanisms of fluid movement into, through and out of the brain: evaluation of the evidence. Fluids Barriers CNS **11**, 26 (2014). https://doi.org/10.1186/2045-8118-11-26
8. Y. Lu, W. Wang, Interaction between the interstitial fluid and the extracellular matrix in confined indentation. J. Biomech. Eng. **130**, 041011 (2008). https://doi.org/10.1115/1.2939310
9. L. Ren, P. Yang, Z. Wang, J. Zhang, C. Ding, P. Shang, Biomechanical and biophysical environment of bone from the macroscopic to the pericellular and molecular level. J. Mech. Behav. Biomed. Mater. **50**, 104 (2015). https://doi.org/10.1016/j.jmbbm.2015.04.021
10. M.K. Lehtinen, M.W. Zappaterra, X. Chen, Y.J. Yang, A. Hill, M. Lun, T. Maynard, D. Gonzalez, S. Kim, P. Ye, A.J. D'Ercole, E.T. Wong, A.S. LaMantia, C.A. Walsh, The cerebrospinal fluid provides a proliferative niche for neural progenitor cells. Neuron **69**, 893 (2011). https://doi.org/10.1016/j.neuron.2011.01.023
11. N. Kaneko, K. Sawamoto, Go with the flow: cerebrospinal fluid flow regulates neural stem cell proliferation. Cell Stem Cell **22**, 783 (2018). https://doi.org/10.1016/j.stem.2018.05.015
12. T. Nakada, I.L. Kwee, Fluid dynamics inside the brain barrier: current concept of interstitial flow, glymphatic flow, and cerebrospinal fluid circulation in the brain. Neuroscientist **25**, 155 (2019). https://doi.org/10.1177/1073858418775027
13. A.K. Shetty, G. Zanirati, The interstitial system of the brain in health and disease. Aging Dis. **11**, 200 (2020). https://doi.org/10.14336/AD.2020.0103
14. N.J. Abbott, Evidence for bulk flow of brain interstitial fluid: significance for physiology and pathology. Neurochem. Int. **45**, 545 (2004). https://doi.org/10.1016/j.neuint.2003.11.006
15. L. Ray, J.J. Iliff, J.J. Heys, Analysis of convective and diffusive transport in the brain interstitium. Fluids Barriers CNS **16**, 6 (2019). https://doi.org/10.1186/s12987-019-0126-9
16. A.P. Haring, H. Sontheimer, B.N. Johnson, Microphysiological human brain and neural systems on a chip: potential alternatives to small animal models and emerging platforms for drug discovery and personalized medicine. Stem Cell Rev. **13**, 381 (2017). https://doi.org/10.1007/s12015-017-9738-0
17. J.-C. Park, S.-Y. Jang, D. Lee, J. Lee, U. Kang, H. Chang, H.J. Kim, S.-H. Han, J. Seo, M. Choi, D.Y. Lee, M.S. Byun, D. Yi, K.-H. Cho, I. Mook-Jung, A logical network-based drug-screening platform for Alzheimer's disease representing pathological features of human brain organoids. Nat. Commun. **12**, 280 (2021). https://doi.org/10.1038/s41467-020-20440-5
18. C. Scopa, F. Marrocco, V. Latina, F. Ruggeri, V. Corvaglia, F. La Regina, M. Ammassari-Teule, S. Middei, G. Amadoro, G. Meli, R. Scardigli, A. Cattaneo, Impaired adult neurogenesis is an early event in Alzheimer's disease neurodegeneration, mediated by intracellular Aβ oligomers. Cell Death Differ. **27**, 934 (2020). https://doi.org/10.1038/s41418-019-0409-3
19. H.S. Kim, S.M. Shin, S. Kim, Y. Nam, A. Yoo, M. Moon, Relationship between adult subventricular neurogenesis and Alzheimer's disease: pathologic roles and therapeutic implications. Front. Aging Neurosci. **14**, 1002281 (2022). https://doi.org/10.3389/fnagi.2022.1002281
20. B. Polis, A.O. Samson, Addressing the discrepancies between animal models and human Alzheimer's disease pathology: implications for translational research. J. Alzheimers Dis. **98**, 1199 (2024). https://doi.org/10.3233/JAD-240058
21. A. Foster-Powell, G. Meno-Tetang, A. Rostami-Hodjegan, K. Ogungbenro, D.E. Mager, Translatability of animal models for Alzheimer's disease using a machine learning based workflow. Clin. Transl. Sci. **18**, e70387 (2025). https://doi.org/10.1111/cts.70387
22. S. Kang, S.E. Park, D.D. Huh, Organ-on-a-chip technology for nanoparticle research. Nano Converg. **8**, 20 (2021). https://doi.org/10.1186/s40580-021-00270-x
23. N.A. Chartrain, M.V. Pryzhkova, J.I. Candelaria, K.H. Gilchrist, P.W. Jordan, An efficient organoid cutting method for long-term culture and high-throughput analyses. Tissue Eng. Regen. Med. **22**, 675 (2025). https://doi.org/10.1007/s13770-025-00731-y
24. M. Shin, T. Ha, S. Lee, C. Li, J.-H. Choi, J.-W. Choi, Biohybrid motor neuron spheroid composed of graphene/HUVEC/neural cell for 3D biosensing

system to evaluate drug of amyotrophic lateral sclerosis. Nano Converg. **12**, 29 (2025). https://doi.org/10.1186/s40580-025-00495-0
25. M. Jorfi, C. D'Avanzo, R.E. Tanzi, D.Y. Kim, D. Irimia, Human neurospheroid arrays for in vitro studies of Alzheimer's disease. Sci. Rep. **8**, 2450 (2018). https://doi.org/10.1038/s41598-018-20436-8
26. Y.J. Choi, S. Chae, J.H. Kim, K.F. Barald, J.Y. Park, S.-H. Lee, Neurotoxic amyloid beta oligomeric assemblies recreated in microfluidic platform with interstitial level of slow flow. Sci. Rep. **3**, 1921 (2013). https://doi.org/10.1038/srep01921
27. Y. Chen, Y. Xu, J. Cai, M. Lauwers, L. Xiang, Y. Zheng, H. Chu, X. Chen, D.F.E. Ker, C. Zhang, D.M. Wang, Z. Zhang, Automated and enclosed three-dimensional biofabrication system for mesenchymal stem cell culture to enhance diabetic wound healing. Biomater. Res. **29**, 0205 (2025). https://doi.org/10.34133/bmr.0205
28. J.Y. Kim, W.-K. Rhim, S.-G. Cha, J. Woo, J.Y. Lee, C.G. Park, D.K. Han, Bolstering the secretion and bioactivities of umbilical cord MSC-derived extracellular vesicles with 3D culture and priming in chemically defined media. Nano Converg. **9**, 57 (2022). https://doi.org/10.1186/s40580-022-00349-z
29. Y. Kang, H. Park, S. Shim, G. Karima, S. Lee, K. Yang, H.D. Kim, MXene nanoparticles: orchestrating spherioidogenesis for targeted osteogenic and neurogenic differentiation. Adv. NanoBiomed Res. **5**, 2400100 (2025). https://doi.org/10.1002/anbr.202400100
30. Q. Ji, Y. Lv, B. Hu, Y. Su, I.I. Shaikh, X. Zhu, Study on the therapeutic potential of induced neural stem cells for Alzheimer's disease in mice. Biol. Res. **57**, 89 (2024). https://doi.org/10.1186/s40659-024-00568-0
31. K. Yang, J.S. Lee, S. Han, Y. Jin, A.-N. Cho, G.-E. Chang, E. Cheong, J.H. Yang, S. Chung, S.-W. Cho, Endothelial-neurosphere crosstalk in microwell arrays regulates self-renewal and differentiation of human neural stem cells. J. Ind. Eng. Chem. **74**, 148 (2019). https://doi.org/10.1016/j.jiec.2019.02.021
32. T.L. Laundos, J. Silva, M. Assunção, P. Quelhas, C. Monteiro, C. Oliveira, M.J. Oliveira, A.P. Pêgo, I.F. Amaral, Rotary orbital suspension culture of embryonic stem cell-derived neural stem/progenitor cells: impact of hydrodynamic culture on aggregate yield, morphology and cell phenotype. J. Tissue Eng. Regen. Med. **11**, 2227 (2017). https://doi.org/10.1002/term.2121
33. J. Seo, J.S. Lee, K. Lee, D. Kim, K. Yang, S. Shin, C. Mahata, H.B. Jung, W. Lee, S. Cho, T. Lee, Switchable water-adhesive, superhydrophobic palladium-layered silicon nanowires potentiate the angiogenic efficacy of human stem cell spheroids. Adv. Mater. **26**, 7043 (2014). https://doi.org/10.1002/adma.201402273
34. R. Duquette, S.P. Salazar, Z.Z. Wang, A. Sohrabi, S.K. Seidlits, Systematic investigation of the effects of neural stem cell spheroid size and density on fate specification in 3D culture. J. Mater. Chem. B **14**, 2014 (2026). https://doi.org/10.1039/d5tb01589h
35. C. Shao, J. Chi, H. Zhang, Q. Fan, Y. Zhao, F. Ye, Development of cell spheroids by advanced technologies. Adv. Mater. Technol. **5**, 2000183 (2020). https://doi.org/10.1002/admt.202000183
36. H. Kim, B. Kim, S.J. Kim, Y. Choi, I.H. Kim, J. Han, Y. Park, Y. Han, J. Park, Reconfigurable hanging drop microarray platform for on-demand preparation and analysis of spheroid array. Adv. Healthc. Mater. **13**, 2400501 (2024). https://doi.org/10.1002/adhm.202400501
37. S. Jang, Y. Park, K.M. Huh, D.Y. Lee, Preparation of highly functional spheroid of endocrine cells based on thermosensitive glycol chitosan. Tissue Eng. Regen. Med. **22**, 309 (2025). https://doi.org/10.1007/s13770-025-00708-x
38. M. Rovere, D. Reverberi, P. Arnaldi, M.E.F. Palamà, C. Gentili, Spheroid size influences cellular senescence and angiogenic potential of mesenchymal stromal cell-derived soluble factors and extracellular vesicles. Front. Bioeng. Biotechnol. **11**, 1297644 (2023). https://doi.org/10.3389/fbioe.2023.1297644
39. C. Eilenberger, M. Rothbauer, F. Selinger, A. Gerhartl, C. Jordan, M. Harasek, B. Schädl, J. Grillari, J. Weghuber, W. Neuhaus, S. Küpcü, P. Ertl, A microfluidic multisize spheroid array for multiparametric screening of anticancer drugs and blood–brain barrier transport properties. Adv. Sci. **8**, 2004856 (2021). https://doi.org/10.1002/advs.202004856
40. D.R. Grimes, F.J. Currell, Oxygen diffusion in ellipsoidal tumour spheroids. J. R. Soc. Interface **15**, 20180256 (2018). https://doi.org/10.1098/rsif.2018.0256
41. M.C. Decarli, M.V. de Castro, J.A. Nogueira, M.H.T. Nagahara, C.B. Westin, A.L.R. de Oliveira, J.V.L. da Silva, L. Moroni, C. Mota, Â.M. Moraes, Development of a device useful to reproducibly produce large quantities of viable and uniform stem cell spheroids with controlled diameters. Biomater. Adv. **135**, 112685 (2022). https://doi.org/10.1016/j.msec.2022.112685
42. E. Lee, A. Chary, Z. Gerelkhuu, P. Weber, I. Virmani, B.A. Brugger, I.R.S. Ribeiro, E. Brun, V. Lacconi, H. Bang, I.H. Kwon, A. Pohl, J. Yoon, S.W. Kim, A.T. Papadiamantis, R.R. Chowdhury, D.-Y. Hwang, L. Lamon, M.-J. Ort, M. Paparella, E.A. Sosnina, A. Serra, J. Morikka, L. Campini, K. Koch, A. Afantitis, D. Greco, I. Lynch, K. Sullivan, S. Yoon, T.G. Lee, J.-W. Park, D.S.T. Martinez, V.P. Dadhania, L. Campagnolo, W. Neuhaus, S. Friedrichs, T. Buerki-Thurnherr, T.H. Yoon, T. Serchi, New approach methodologies for next-generation risk assessment of nanomaterials and nano-enabled products. Nano Converg. (2026). https://doi.org/10.1186/s40580-026-00566-w
43. C. Li, J. Pan, Z. Shi, X. Zeng, X. Xia, X. He, W. Wang, B. Qiu, W. Ding, D. Huang, Engineered endometrial clear cell cancer-on-a-chip reveals early invasion-metastasis cascade of cancer cells. Biomater. Res. **29**, 0177 (2025). https://doi.org/10.34133/bmr.0177
44. L. van Os, J. Yeoh, G. Witz, D. Ferrari, P. Krebs, Y. Chandorkar, S. Zeinali, A. Sengupta, O.T. Guenat, Immune cell extravasation in an organ-on-chip to model lung inflammation. Eur. J. Pharm. Sci. **187**, 106485 (2023). https://doi.org/10.1016/j.ejps.2023.106485
45. J.H. Kim, Brain-derived neurotrophic factor exerts neuroprotective actions against amyloid β-induced apoptosis in neuroblastoma cells. Exp. Ther. Med. **8**, 1891 (2014). https://doi.org/10.3892/etm.2014.2033
46. S. Arancibia, M. Silhol, F. Moulière, J. Meffre, I. Höllinger, T. Maurice, L. Tapia-Arancibia, Protective effect of BDNF against beta-amyloid induced neurotoxicity in vitro and in vivo in rats. Neurobiol. Dis. **31**, 316 (2008). https://doi.org/10.1016/j.nbd.2008.05.012
47. E.V. Mitroshina, R.S. Yarkov, T.A. Mishchenko, V.G. Krut', M.S. Gavrish, E.A. Epifanova, A.A. Babaev, M.V. Vedunova, Brain-derived neurotrophic factor (BDNF) preserves the functional integrity of neural networks in the β-amyloidopathy model in vitro. Front. Cell. Dev. Biol. **8**, 582 (2020). https://doi.org/10.3389/fcell.2020.00582
48. L. Gao, Y. Zhang, K. Sterling, W. Song, Brain-derived neurotrophic factor in Alzheimer's disease and its pharmaceutical potential. Transl. Neurodegener. **11**, 4 (2022). https://doi.org/10.1186/s40035-022-00279-0
49. C. Géral, A. Angelova, S. Lesieur, From molecular to nanotechnology strategies for delivery of neurotrophins: emphasis on brain-derived neurotrophic factor (BDNF). Pharmaceutics **5**, 127 (2013). https://doi.org/10.3390/pharmaceutics5010127
50. Z. Shi, Z. Fan, H. Zhang, S. Li, H. Yuan, J. Tong, Localized delivery of brain-derived neurotrophic factor from PLGA microspheres promotes peripheral nerve regeneration in rats. J. Orthop. Surg. Res. **17**, 172 (2022). https://doi.org/10.1186/s13018-022-02985-x
51. H. Lee, M.-J. Kim, D. Kim, C.H. Moon, S. Bang, H.S. Kang, J.Y. Gwon, J.H. Seo, J. Jeon, J. Son, M. Lim, M. Kang, D.Y. Lee, D. Lim, J.-H. Park, G.D. Cha, S.-H. Lee, T.-S. Jang, K. Yang, Y. Jeong, Y. Eom, H.-D. Jung, AI–guided 4D printing of carnivorous plants–inspired microneedles for accelerated wound healing. Adv. Mater. **38**, e23665 (2026). https://doi.org/10.1002/adma.202523665
52. Y. Jun, J. Lee, S. Choi, J.H. Yang, M. Sander, S. Chung, S.-H. Lee, In vivo–mimicking microfluidic perfusion culture of pancreatic islet spheroids. Sci. Adv. **5**, eaax4520 (2019). https://doi.org/10.1126/sciadv.aax4520
53. E.-Y. Koo, K.-H. Park, S.-W. Kang, K.-M. Huh, Design and evaluation of hexanoyl glycol chitosan-based ultra-low attachment mesh-pattern culture dishes for 3D cell culture. Polymer **47**, 369 (2023). https://doi.org/10.7317/pk.2023.47.3.369
54. B.T. Fuller, T.H. Jones, E.T. Chan, M.W. D'Souza, K.E. Luker, G.D. Luker, J.W. Song, Quantitative spatiotemporal analysis of intracellular kinase activity in metastatic breast cancer cells using a microfluidic-based lateral diffusion assay. Anal. Chem. **98**, 18607 (2026). https://doi.org/10.1021/acs.analchem.6c01060
55. M.M. Ferreira, R.E. Dewi, S.C. Heilshorn, Microfluidic analysis of extracellular matrix-bFGF crosstalk on primary human myoblast chemoproliferation, chemokinesis, and chemotaxis. Integr. Biol. **7**, 569 (2015). https://doi.org/10.1039/c5ib00060b
56. K. An, I. Klyubin, Y. Kim, J.H. Jung, A.J. Mably, S.T. O'Dowd, T. Lynch, D. Kanmert, C.A. Lemere, G.M. Finan, J.W. Park, T.-W. Kim, D.M. Walsh, M.J. Rowan, J.-H. Kim, Exosomes neutralize synaptic-plasticity-disrupting activity of Aβ assemblies in vivo. Mol. Brain **6**, 47 (2013). https://doi.org/10.1186/1756-6606-6-47
57. W.B. Stine, L. Jungbauer, C. Yu, M.J. LaDu, Preparing synthetic Aβ in different aggregation states. Methods Mol. Biol. **670**, 13 (2011). https://doi.org/10.1007/978-1-60761-744-0_2
58. D.J. Garzon, M. Fahnestock, Oligomeric amyloid decreases basal levels of brain-derived neurotrophic factor (BDNF) mRNA via specific downregulation of BDNF transcripts IV and V in differentiated human neuroblastoma cells. J. Neurosci. **27**, 2628 (2007). https://doi.org/10.1523/JNEUROSCI.5053-06.2007
59. C. Kim, H. Kim, W.-S. Sim, M. Jung, J. Hong, S. Moon, J.-H. Park, J.-J. Kim, M. Kang, S. Kwon, M.-J. Kim, K. Ban, H.-J. Park, B.-S. Kim, Spatiotemporal control of neutrophil fate to tune inflammation and repair for myocardial infarction therapy. Nat. Commun. **15**, 8481 (2024). https://doi.org/10.1038/s41467-024-52812-6

60. J. Kim, J. Bae, B. Cui, S.-W. Cho, K. Yang, A convective transport-enhanced multi-organoid device for therapeutic modeling of the liver-pancreas axis in obesity. Theranostics **16**, 220 (2026). https://doi.org/10.7150/thno.114415
61. K. Yang, S. Han, Y. Shin, E. Ko, J. Kim, K.I. Park, S. Chung, S.-W. Cho, A microfluidic array for quantitative analysis of human neural stem cell self-renewal and differentiation in three-dimensional hypoxic microenvironment. Biomaterials **34**, 6607 (2013). https://doi.org/10.1016/j.biomaterials.2013.05.067
62. S. Chen, Y. Zhou, Y. Chen, Gu, fastp: an ultra-fast all-in-one FASTQ preprocessor. Bioinformatics. **34**, i884 (2018). https://doi.org/10.1093/bioinformatics/bty560
63. A. Dobin, C.A. Davis, F. Schlesinger, J. Drenkow, C. Zaleski, S. Jha, P. Batut, M. Chaisson, T.R. Gingeras, STAR: ultrafast universal RNA-seq aligner. Bioinformatics **29**, 15 (2013). https://doi.org/10.1093/bioinformatics/bts635
64. Y. Liao, G.K. Smyth, W. Shi, featureCounts: an efficient general purpose program for assigning sequence reads to genomic features. Bioinformatics **30**, 923 (2014). https://doi.org/10.1093/bioinformatics/btt656
65. Y. Chen, L. Chen, A.T.L. Lun, P.L. Baldoni, G.K. Smyth, edgeR v4: powerful differential analysis of sequencing data with expanded functionality and improved support for small counts and larger datasets. Nucleic Acids Res. **53**, gkaf018 (2025). https://doi.org/10.1093/nar/gkaf018
66. B.T. Sherman, M. Hao, J. Qiu, X. Jiao, M.W. Baseler, H.C. Lane, T. Imamichi, W. Chang, DAVID: a web server for functional enrichment analysis and functional annotation of gene lists (2021 update). Nucleic Acids Res. **50**, W216 (2022). https://doi.org/10.1093/nar/gkac194
67. K. Yang, J.Y. Oh, J.S. Lee, Y. Jin, G.-E. Chang, S.S. Chae, E. Cheong, H.K. Baik, S.-W. Cho, Photoactive poly(3-hexylthiophene) nanoweb for optoelectrical stimulation to enhance neurogenesis of human stem cells. Theranostics **7**, 4591 (2017). https://doi.org/10.7150/thno.20169
68. B.S. Jang, K.H. Park, E.Y. Suh, B.-S. Lee, S.-W. Kang, K.M. Huh, Non-cell adhesive hexanoyl glycol chitosan hydrogels for stable and efficient formation of 3D cell spheroids with tunable size and density. Int. J. Biol. Macromol. **187**, 955 (2021). https://doi.org/10.1016/j.ijbiomac.2021.07.185
69. D.-E. Kim, Y.B. Lee, H.-E. Shim, J.J. Song, J.-S. Han, K.-S. Moon, K.M. Huh, S.-W. Kang, Application of hexanoyl glycol chitosan as a non-cell adhesive polymer in three-dimensional cell culture. ACS Omega **7**, 18471 (2022). https://doi.org/10.1021/acsomega.2c00890
70. S. Islam, J. Parker, B.C. Dash, H.C. Hsia, Human iPSC-vascular smooth muscle cell spheroids demonstrate size-dependent alterations in cellular viability and secretory function. J. Biomed. Mater. Res. A **110**, 1813 (2022). https://doi.org/10.1002/jbm.a.37423
71. Y. Juste-Lanas, S. Hervas-Raluy, J.M. García-Aznar, A. González-Loyola, Fluid flow to mimic organ function in 3D in vitro models. APL Bioeng. **7**, 031501 (2023). https://doi.org/10.1063/5.0146000
72. M.A. Winkelman, D.Y. Kim, S. Kakarla, A. Grath, N. Silvia, G. Dai, Interstitial flow enhances the formation, connectivity, and function of 3D brain microvascular networks generated within a microfluidic device. Lab. Chip. **22**, 170 (2022). https://doi.org/10.1039/D1LC00605C
73. C. Watson, C. Liu, A. Ansari, H.C. Miranda, R.A. Somoza, S.E. Senyo, Multiplexed microfluidic chip for cell co-culture. Analyst **147**, 5409 (2022). https://doi.org/10.1039/d2an01344d
74. J.Y. Kim, J.-H. Lee, W. Sun, Isolation and culture of adult neural stem cells from the mouse subcallosal zone. J. Vis. Exp. **118**, e54929 (2016). https://doi.org/10.3791/54929
75. C. Rathnam, L. Yang, S. Castro-Pedrido, J. Luo, L. Cai, K.-B. Lee, Hybrid SMART spheroids to enhance stem cell therapy for CNS injuries. Sci. Adv. **7**, eabj2281 (2021). https://doi.org/10.1126/sciadv.abj2281
76. H. Hampel, J. Hardy, K. Blennow, C. Chen, G. Perry, S.H. Kim, V.L. Villemagne, P. Aisen, M. Vendruscolo, T. Iwatsubo, C.L. Masters, M. Cho, L. Lannfelt, J.L. Cummings, A. Vergallo, The amyloid-β pathway in Alzheimer's disease. Mol. Psychiatry **26**, 5481 (2021). https://doi.org/10.1038/s41380-021-01249-0
77. T.K.S. Ng, C.S.H. Ho, W.W.S. Tam, E.H. Kua, R.C.-M. Ho, Decreased serum brain-derived neurotrophic factor (BDNF) levels in patients with Alzheimer's disease (AD): a systematic review and meta-analysis. Int. J. Mol. Sci. **20**, 257 (2019). https://doi.org/10.3390/ijms20020257
78. H.K. Makadia, S.J. Siegel, Poly lactic-co-glycolic acid (PLGA) as a biodegradable controlled drug delivery carrier. Polymers **3**, 1377 (2011). https://doi.org/10.3390/polym3031377
79. S. Bohrey, V. Chourasiya, A. Pandey, Polymeric nanoparticles containing diazepam: preparation, optimization, characterization, in-vitro drug release and release kinetic study. Nano Converg. **3**, 3 (2016). https://doi.org/10.1186/s40580-016-0061-2
80. C.J. Garwood, A.M. Pooler, J. Atherton, D.P. Hanger, W. Noble, Astrocytes are important mediators of Aβ-induced neurotoxicity and tau phosphorylation in primary culture. Cell. Death Dis. **2**, e167 (2011). https://doi.org/10.1038/cddis.2011.50
81. Y. Zhang, H. Chen, R. Li, K. Sterling, W. Song, Amyloid β-based therapy for Alzheimer's disease: challenges, successes and future. Signal. Transduct. Target. Ther. **8**, 248 (2023). https://doi.org/10.1038/s41392-023-01484-7
82. D.A. Butterfield, Amyloid β-peptide (1–42)-induced oxidative stress and neurotoxicity: implications for neurodegeneration in Alzheimer's disease brain. A review. Free Radic. Res. **36**, 1307 (2002). https://doi.org/10.1080/10715760210000049890
83. Y. Gasca-Martínez, M.A. Ontiveros-Torres, I. López-Gallegos, J.J. Jarero-Basulto, Amyloid beta oligomers as early triggers of neuronal cytoskeleton dysfunction in Alzheimer's disease. Pathophysiology. **33**, 14 (2026). https://doi.org/10.3390/pathophysiology33010014
84. L. Mucke, D.J. Selkoe, Neurotoxicity of amyloid β-protein: synaptic and network dysfunction. Cold Spring Harb. Perspect. Med. **2**, a006338 (2012). https://doi.org/10.1101/cshperspect.a006338
85. P. Obexer, J. Hagenbuchner, T. Unterkircher, N. Sachsenmaier, C. Seifarth, G. Böck, V. Porto, K. Geiger, M. Ausserlechner, K. Luo, Repression of BIRC5/Survivin by FOXO3/FKHRL1 sensitizes human neuroblastoma cells to DNA damage-induced apoptosis. Mol. Biol. Cell **20**, 2041 (2009). https://doi.org/10.1091/mbc.e08-07-0699
86. A.H. Stegh, H. Kim, R.M. Bachoo, K.L. Forloney, J. Zhang, H. Schulze, K. Park, G.J. Hannon, J. Yuan, D.N. Louis, R.A. DePinho, L. Chin, Bcl2L12 inhibits post-mitochondrial apoptosis signaling in glioblastoma. Genes Dev. **21**, 98 (2007). https://doi.org/10.1101/gad.1480007
87. R.R. Crawford, E.T. Prescott, C.F. Sylvester, A.N. Higdon, J. Shan, M.S. Kilberg, I.N. Mungrue, Human CHAC1 protein degrades glutathione, and mRNA induction is regulated by the transcription factors ATF4 and ATF3 and a bipartite ATF/CRE regulatory element. J. Biol. Chem. **290**, 15878 (2015). https://doi.org/10.1074/jbc.M114.635144
88. Z. Gu, H. Cao, C. Zuo, Y. Huang, J. Miao, Y. Song, Y. Yang, L. Zhu, F. Wang, TFEB in Alzheimer's disease: from molecular mechanisms to therapeutic implications. Neurobiol. Dis. **173**, 105855 (2022). https://doi.org/10.1016/j.nbd.2022.105855
89. Y. Ben Zablah, H. Zhang, R. Gugustea, Z. Jia, LIM kinases in synaptic plasticity, memory, and brain diseases. Cells **10**, 2079 (2021). https://doi.org/10.3390/cells10082079
90. K.I. Gidado, F.O. Adeshakin, L. Rabiu, Z. Zhang, G. Zhang, X. Wan, Multifaceted roles of DLG3/SAP102 in neurophysiology, neurological disorders and tumorigenesis. Neuroscience. **565**, 192 (2025). https://doi.org/10.1016/j.neuroscience.2024.11.081
91. D. Su, H. Liu, T. Liu, X. Zhang, W. Yang, Y. Song, J. Liu, Y. Wu, L. Chang, Dynamic SAP102 expression in the hippocampal subregions of rats and APP/PS1 mice of various ages. J. Anat. **232**, 987 (2018). https://doi.org/10.1111/joa.12807
92. H. Haytural, T. Jordà-Siquier, B. Winblad, C. Mulle, L.O. Tjernberg, A.-C. Granholm, S. Frykman, G. Barthet, Distinctive alteration of presynaptic proteins in the outer molecular layer of the dentate gyrus in Alzheimer's disease. Brain Commun. **3**, fcab079 (2021). https://doi.org/10.1093/braincomms/fcab079
93. P. Kowiański, G. Lietzau, E. Czuba, M. Waśkow, A. Steliga, J. Moryś, BDNF: a key factor with multipotent impact on brain signaling and synaptic plasticity. Cell. Mol. Neurobiol. **38**, 579 (2018). https://doi.org/10.1007/s10571-017-0510-4
94. P. Sanphui, S.C. Biswas, FoxO3a is activated and executes neuron death via Bim in response to β-amyloid. Cell Death Dis. **4**, e625 (2013). https://doi.org/10.1038/cddis.2013.148
95. Y. Ohyagi, H. Asahara, D.-H. Chui, Y. Tsuruta, N. Sakae, K. Miyoshi, T. Yamada, H. Kikuchi, T. Taniwaki, H. Murai, K. Ikezoe, H. Furuya, T. Kawarabayashi, M. Shoji, F. Checler, T. Iwaki, T. Makifuchi, K. Takeda, J.-I. Kira, T. Tabira, Intracellular Aβ42 activates p53 promoter: a pathway to neurodegeneration in Alzheimer's disease. FASEB J. **19**, 1 (2005). https://doi.org/10.1096/fj.04-2637fje
96. J. Zhu, C. Wu, L. Yang, Cellular senescence in Alzheimer's disease: from physiology to pathology. Transl Neurodegener. **13**, 55 (2024). https://doi.org/10.1186/s40035-024-00447-4
97. S.H. Berth, T.E. Lloyd, Disruption of axonal transport in neurodegeneration. J. Clin. Invest. **133**, e168554 (2023). https://doi.org/10.1172/JCI168554
98. J. Park, B.K. Lee, G.S. Jeong, J.K. Hyun, C.J. Lee, S.-H. Lee, Three-dimensional brain-on-a-chip with an interstitial level of flow and its application as an in vitro model of Alzheimer's disease. Lab. Chip. **15**, 141 (2014). https://doi.org/10.1039/C4LC00962B

99. Q. Deng, C. Wu, E. Parker, T.C.-Y. Liu, R. Duan, L. Yang, Microglia and astrocytes in Alzheimer's disease: significance and summary of recent advances. Aging Dis. **15**, 1537 (2024). https://doi.org/10.14336/AD.2023.0907

Publisher's note

Springer Nature remains neutral with regard to jurisdictional claims in published maps and institutional affiliations.